

Università degli Studi di Trieste

Facoltà di Scienze Matematiche, Fisiche e Naturali
Corso di Laurea Specialistica in Fisica

Tesi di Laurea

Toward a comprehensive picture of the orbital polarization and the magnetic properties of ruthenates

Verso una descrizione completa degli effetti di polarizzazione orbitale e delle proprietà magnetiche dei rutenati

Relatore:
Prof. Fulvio Parmigiani
Correlatore:
Dott. Marco Malvestuto

Candidato:
Lorenzo Galli

A.A. 2009/2010

To my parents, Daniela and Valentino

Riassunto

In questa tesi vengono presentati i risultati di uno studio delle proprietà magnetiche ed elettroniche dei primi tre membri della serie di Ruddlesden-Popper di ossidi di stronzio-rutenio, $Sr_{n+1}Ru_nO_{3n+1}$. Questi composti appartengono alla più ampia classe di ossidi di metalli di transizione $4d$, nei quali gli effetti di campo cristallino e di scambio (*exchange*) sono in competizione nel determinare le proprietà fisiche dei composti, avendo energie compatibili. Infatti, le variazioni della struttura cristallina, e quindi della sovrapposizione tra gli orbitali atomici, portano ad una competizione tra gli stati fondamentali (*ground states*) dei sistemi studiati, che si manifesta in un'ampia gamma di comportamenti elettronici e magnetici. Nel caso della serie di rutenati studiati, ad esempio, le proprietà fisiche dipendono principalmente dal numero di piani ottaedrici $Ru - O_2$ contenuti nella cella unitaria, e sono associati ad una graduale riduzione delle simmetrie presenti in quest'ultima.

In particolare, lo studio presentato in questa tesi si è focalizzato sulla transizione da un comportamento elettronico di liquido di Fermi ad uno di liquido non-Fermi, che prende luogo nel secondo e terzo membro della serie ad una temperatura di circa $20\,K$. Adoperando la tecnica sperimentale dell'assorbimento dicroico circolare magnetico (XMCD) sulla soglia di assorbimento $L_2(2p - 4d)$ dello ione rutenio, si è studiato lo stato magnetico del composto $Sr_4Ru_3O_{10}$, in funzione della temperatura e del campo magnetico applicato. Si è invece utilizzata la tecnica della variazione della reflettivià risolta in tempo per esaminare il comportamento dinamico della reflettività di $Sr_3Ru_2O_7$ in funzione della temperatura, senza l'utilizzo di un campo magnetico. I risultati di questi due approcci sperimentali differenti hanno

permesso di riprodurre in parte i diagrammi di fase dei materiali lungo le transizioni elettroniche d'interesse, confermando precedenti risultati in letteratura e offrendo spunti per una descrizione più completa del comportamento elettronico e magnetico nei dintorni delle transizioni. Si è infine analizzato la diversa geometria orbitale di Sr_2RuO_4 e $Sr_4Ru_3O_{10}$ attraverso uno studio dell'eccitazione di scambio di carica tra gli orbitali ibridizzati $O\,2p - Ru\,4d$, che formano la banda di valenza dei due composti. Con la tecnica dell'emissione di raggi-X risonante (RXES) attraverso la soglia di assorbimento K ($1s-2p$) dell'ossigeno, si è trovata una dipendenza dell'eccitazione di scambio dalla densità di stati elettronici dei campioni, la cui diversità rispecchia l'inequivalenza dei legami $Ru-O$, dovuta principalmente alle distorsioni presenti nelle due celle unitarie.

Aim of this thesis

In this thesis I present a study of the electronic and magnetic properties of the first three members of the Strontium-Ruthenium oxides of the Ruddlesden-Popper (R-P) series, $Sr_{n+1}Ru_nO_{3n+1}$. I made use of three different experimental techniques, namely: X-ray Magnetic Circular Dichroism (XMCD), time-resolved Reflectivity, and Resonant X-ray Emission Spectroscopy (RXES). I will report the experimental data of these techniques and I will discuss the results of the analysis of the data in the light of the more general open questions still pending on the physical properties of these systems. In particular, the present work has focused on the similar properties governing the ground states of $Sr_3Ru_2O_7$ and $Sr_4Ru_3O_{10}$, for example the transition between Fermi-liquid (FL) and non-Fermi-liquid (NFL) electronic states, which reflects on several physical properties.

I studied the electronic and magnetic properties of these compounds around the critical parameter values, i.e. magnetic field and temperature, in order to reproduce portions of their phase diagrams, using different experimental techniques. In particular, I took part in an XMCD experiment being carried out to study the long range ferromagnetic ordering and the metamagnetic transition of the $Sr_4Ru_3O_{10}$ compound. I also participate in a time-resolved reflectivity experiment whose aims were to investigate the electronic properties of $Sr_3Ru_2O_7$, across the FL-NFL transition. The most important experimental results achieved during this work are: first, the measurement of magnetization curves of the $Sr_4Ru_3O_{10}$ compound as a function of temperature and magnetic field's magnitude and orientation across the metamagnetic transition. Secondly, the time-resolved reflectivity measurements as a function of the temperature, showing that the FL-NFL

behaviour is not associated with a structural transition. Finally, the RXES measurements allowed to make a direct comparison between the valence and conduction band of the first and the third member of the R-P series with a RXES experiment, showing that local electronic structure is strongly affected by the number n of $Ru-O$ layers.

This thesis is organized as follows: in the first chapter, the state-of-art knowledge in the physical properties of the first three R-P ruthenates is described, and the principal open questions are underlined. The second chapter deals with the experimental playgrounds and the theoretical models used in each experimental analysis. In the third chapter the experimental set-ups are described. The analysis and the discussions of the obtained results are the subjects of the fourth chapter. In the last (fifth) chapter conclusions are summarized.

Contents

1 Introduction **1**

1.1 Correlated electron systems 1

1.2 R-P ruthenates 2

1.2.1 Sr_2RuO_4 3

1.2.2 $Sr_3Ru_2O_7$ 4

1.2.3 $Sr_4Ru_3O_{10}$ 6

2 Theoretical models **9**

2.1 Time-resolved Reflectivity: Two-temperature model 9

2.2 X-ray Magnetic Circular Dichroism (XMCD) 11

2.2.1 XMCD effect in $L_{2,3}$ edges 11

2.2.2 Two step model 13

2.3 Resonant X-ray emission spectroscopy (RXES) 15

2.3.1 Connection between RXES and DOS of conduction band 17

3 Experimental set-ups **19**

3.1 Time-resolved Reflectivity 19

3.1.1 Experimental set-up 20

3.2 XMCD 23

3.2.1 Set-up 23

3.3 RXES 25

3.3.1 Experimental set-up 25

4 Data analysis and discussion of results **27**
4.1 Time-resolved reflectivity 27
4.1.1 Description of the data 27
4.1.2 Data analysis and discussion 33
4.2 XMCD 37
4.2.1 Data analysis 37
4.2.2 Discussion 42
4.3 RXES data analysis 44
4.3.1 X-ray absorption spectra 44
4.3.2 RXES spectra 45
4.3.3 Comparison between RXES spectra and simulated DOS 49

5 Conclusions **53**

Appendix **55**
Three-temperature model 55

Bibliography **57**

Chapter 1

Introduction

1.1 Correlated electron systems

In solid state physics, an open field of research deals with strongly correlated electron systems, i.e. compounds whose physical properties are dominated by strong electron-electron ($e-e$) interactions. This is the case where the on-site $e-e$ repulsion is much larger than the energies associated to the overlap of atomic orbitals belonging to different atoms. Electronic correlations can give rise to a large variety of different phenomena, i.e. high-temperature superconductivity in cuprates[1], orbital ordering in manganites[2], and also exotic magnetic behavior such as metamagnetic transitions[3]. A particular class of strongly correlated materials are the $3d$ transition metal oxides (TMOs), where interesting physical phenomena originate from the competition between the local nature of $3d$ orbitals and their narrow bandwidth. Transition metal ions are often characterized with the strength of the exchange splitting energy, compared to that originating from crystal field effect and spin-orbit coupling[4].

This thesis deals with a particular class of materials, belonging to the $4d$ TMOs family: the Strontium-Ruthenium oxides of the Ruddlesden-Popper (R-P) series, $Sr_{n+1}Ru_nO_{3n+1}$(see figure 1.1). The electronic structure of $4d$ TMOs is quite different from that of the more studied $3d$ TMOs, and usually correlation effects are expected to be less pronounced. In fact, the $4d$

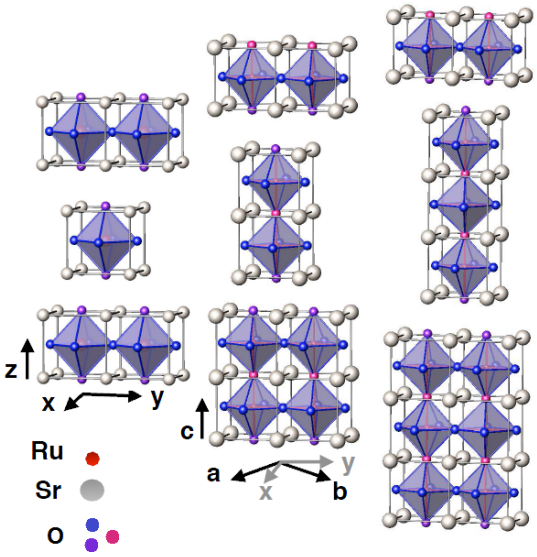


Figure 1.1: *The first three members of the Ruddlesden-Popper series. From left to right:* Sr_2RuO_4 , $Sr_3Ru_2O_7$, $Sr_4Ru_3O_{10}$.

orbitals are more extended in space, and thus the crystal field splitting is usually larger than the exchange splitting[4].
Nevertheless, Strontium-Ruthenium oxides of the R-P series are a particular class of $4d$ materials, in which electronic correlations are unusually strong. Their ground states, indeed, cover a wide range of behaviors, despite the fact that only small crystal distortions occurs between the series. In particular, their physical properties strongly depend on the number n of RuO_2 octahedral layers. Understanding how the change in the principal order parameter n modifies spin and lattice properties is then crucial to explain the physics of these correlated electron systems.

1.2 R-P ruthenates

Ground state properties of Sr-ruthenates depend strongly on the purity of the sample. In recent years, new growing techniques allow the realization of high purity crystals[5], whose physical behaviours were often found to deviate from previously and less pure samples. The degree of purity decrease with

the size and complexity of the primitive cell, so many open questions and diatribes in the scientific scenario reside, for this reason, especially in the more complex $Sr_3Ru_2O_7$ and $Sr_4Ru_3O_{10}$ compounds. The samples studied were grown using the floating-zone technique[5], which allows the best degree of purity currently available.

In the following subsections a brief review of the physical properties is presented, for each of the studied compound, and the state-of-art knowledge is described.

1.2.1 Sr_2RuO_4

Sr_2RuO_4 is the first member of R-P type ruthenates series, and it is also the most studied ruthenate, since the discovery of superconductivity below $T_c \simeq 1.5\,K$ [6]. The crystal structure of this compound belongs to the $I4/mmm$ body-centered tetragonal space-group symmetry, as sketched in figure 1.1, with low-temperature lattice parameters $a = b = 3.862\,\text{Å}$ and $c = 12.722\,\text{Å}$. It doesn't present any phase transitions up to room temperature.

The peculiarities of this ruthenate are: an unconventional nature of superconductivity with strong experimental evidences of a p-wave spin-triplet pairing[1] and a quasi-2D Fermi-liquid behaviour in the ab plane, with highly anisotropic electrical conductivity (see figure 1.2). A complete review of its physical properties can be found in Ref.[7]. It is considered a very important material, since it can be easily grown with high purity and since it can be easily compared with the copper related ($3d$) superconductors[8, 9].

[1] In crystalline solids it's in widespread use symmetries in spin and orbital angular momentum, although they are no more good quantum numbers. The nomenclature refers to the type of symmetry-breaking properties of the condensate, with respect to the gap function as the order parameter. A conventional superconductors can be described with the BCS theory, in which the Cooper pairs are in s-wave.

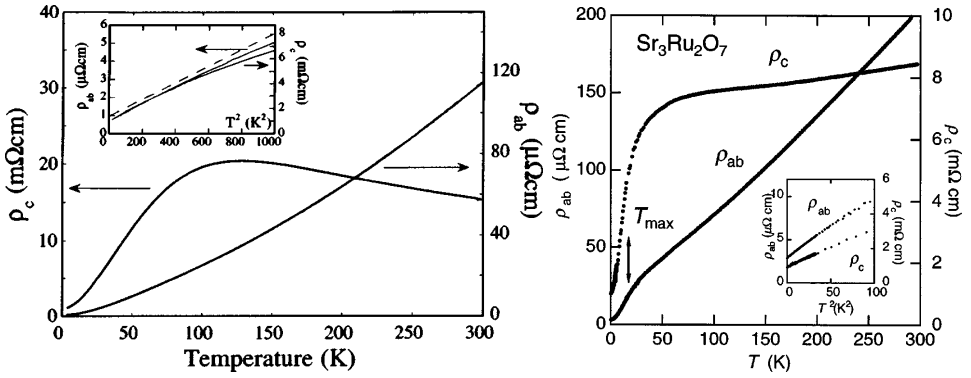


Figure 1.2: *On the left: anisotropic resistivity in Sr_2RuO_4. Image taken from Ref.[10]. On the right: the electrical resistivity of $Sr_3Ru_2O_7$; image taken from Ref.[11]. In both the insets, the low-temperature T^2 dependence of resistivity, expected of a Fermi liquid.*

1.2.2 $Sr_3Ru_2O_7$

$Sr_3Ru_2O_7$ is the $n = 2$ member of R-P type ruthenates series. The RuO_6 octahedra inside the unit cell of $Sr_3Ru_2O_7$ are rotated by $\sim 7°$ along the c axis, due to the double layer structure, which cause compressions in the equatorial plane and a cooperative bending of the oxygen bond, shared by the octahedra [12]. Hence the final structure is a distorted rock-salt, belonging to the *Bbcb* space group, with $a \simeq b = 3.8872\,\text{Å}$ and $c = 20.732\,\text{Å}$.

The physics of this compound can be described looking at the figure 1.2: $Sr_3Ru_2O_7$ is a quasi-2D metal, with $\rho_c/\rho_{ab} \simeq 300$ at room temperature, reflecting the layered character of its crystal structure. A remarkable decrease of ρ_c is present below $50\,K$, and a Fermi-liquid state is present up to $10\,K$, as stressed in the inset. This behaviour is caused by a competition in the ground state between a ferromagnetic (FM) ordering and antiferromagnetic (AFM) correlation effects, as underlined by Ref[13, 14]. $Sr_3Ru_2O_7$ is indeed an enhanced paramagnet (or nearly ferromagnet), i.e. it doesn't present neither a long range FM nor a AFM ordering [15, 11, 16]. In particular, Capogna in Ref.[16] shows that the change in temperature of magnetic fluctuations is reflected in macroscopic properties, such as the magnetic susceptibility (see figure 1.3). Here, the AFM fluctuations fall away rapidly with increasing temperature, and participate predominantly up to $\sim 20\,K$. The transition

occurring at this temperature is still not well defined, and will be analyzed in this thesis. In figure 1.4(a), the behaviour of the resistivity is sketched as a function of temperature and on applied external magnetic field H. We can see that the transition occurring at $\sim 15\,K$ and zero field is accompanied by a change in the resistivity behaviour, from Fermi-liquid to a more complicated one. The effect of increasing H drives this transition to lower temperatures, eventually terminated in a quantum critical point [17, 3], as sketched in the phase diagram in figure 1.4(b).

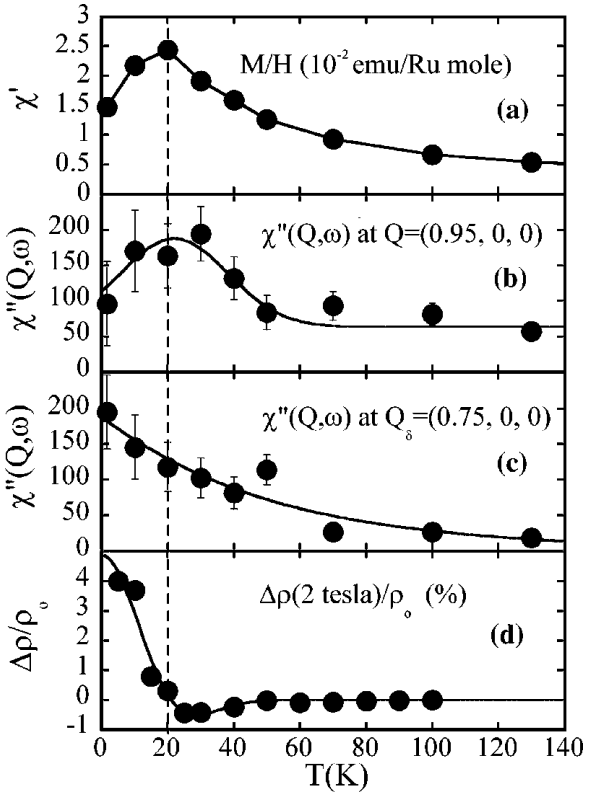


Figure 1.3: *Temperature-dependence of the magnetic response from macroscopic and microscopic measurements, taken from Ref.[16]. In (a) the static susceptibility,as measured from Ref.[11]; in (b) the susceptibility from neutron scattering, close to a FM position, at an energy transfer of* $2\,meV$*; in (c) the same physical quantity for an AFM position; in (d) the the fractional longitudinal magneto-resistance under applied magnetic field parallel to the ab plane. The dashed line at* $\sim 20\,K$ *marks the suppression of the AFM behaviour, dominant at low temperatures.*

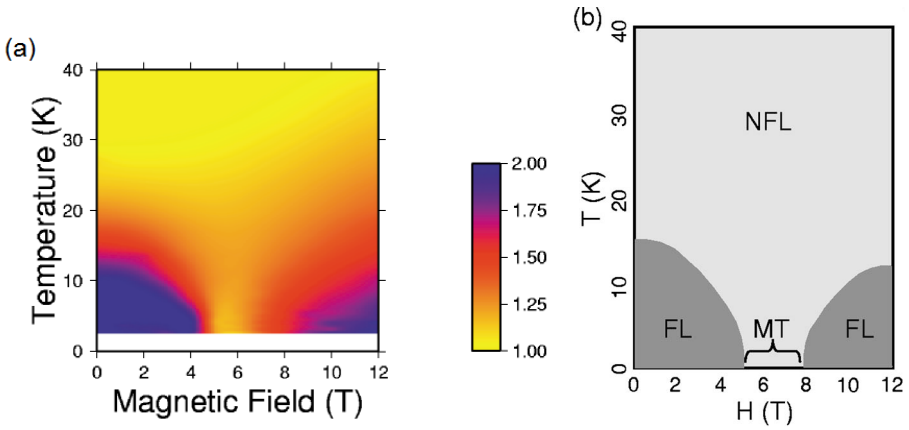


Figure 1.4: *(a): the evolution of the temperature dependence of the resistivity of* $Sr_3Ru_2O_7$ *as a function of temperature, with* $B \| I \| ab$*, where* I *is the current, for different applied magnetic field. The colors represent the value of the* α *coefficient for the proportionality:* $\rho \propto T^{\alpha}$*. Taken from Ref.[18]. (b): phase diagram showing the temperature and magnetic field dependent crossover between a Fermi-liquid (FL) and non-Fermi-liquid (NFL) behavior in* $Sr_3Ru_2O_7$ *[15], separated by a low temperature metamagnetic (MT) transition range.*

1.2.3 $Sr_4Ru_3O_{10}$

The triple-layer $Sr_4Ru_3O_{10}$ is a structurally distorted ferromagnet, with a Curie temperature of $T_C = 105K$. Distortions take place differently in the $Ru{-}O{-}Ru$ angle of planar octahedra, as sketched in figure 1.5. As the sister compounds, resistivities exhibit a Fermi liquid behaviour up to $15\,K$, with a strong, but less marked, anisotropy (figure 1.6(b)).

Magnetization measurements versus applied magnetic field show that $Sr_4Ru_3O_{10}$ has a FM ordering along the c axis, while in the basal plane it presents a sharp metamagnetic transition, B_C, up to $50\,K$ (figure 1.8).

First measurements as a function of temperature show that the FM transition at T_C is followed by an additional magnetic transition at $T_M \simeq 50\,K$, that is visible also in the trend of the out-of-plane resistivity (1.6). Although this behaviour was first thought as that of an AFM transition, with a canted out-of plane spin orientation [19], recent neutron scattering measurements [20] show that the magnetic structure must follows the same symmetry of the crystal structure, and the spin's easy axes lie in the ab plane. The mag-

netic behaviour along the *ab* plane is described in the phase diagram of figure 1.7.

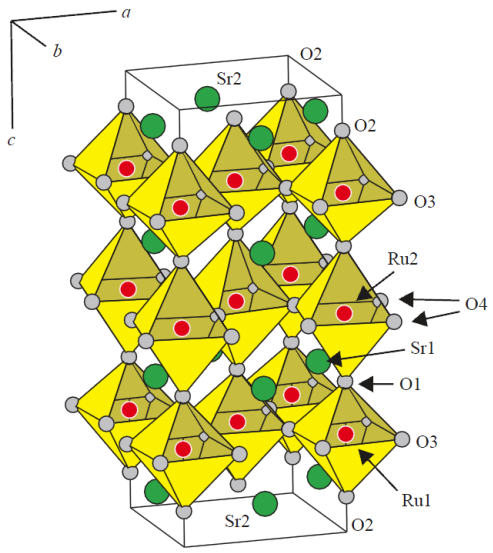


Figure 1.5: *Simplified distorted structure of $Sr_4Ru_3O_{10}$, as in Ref. [21]. In the outer layers octahedra are rotated along the c axis of $\sim 5.6^\circ$, in the central layers of $\sim 11^\circ$ in the opposite direction. The symmetry group is $P4/mbm$.*

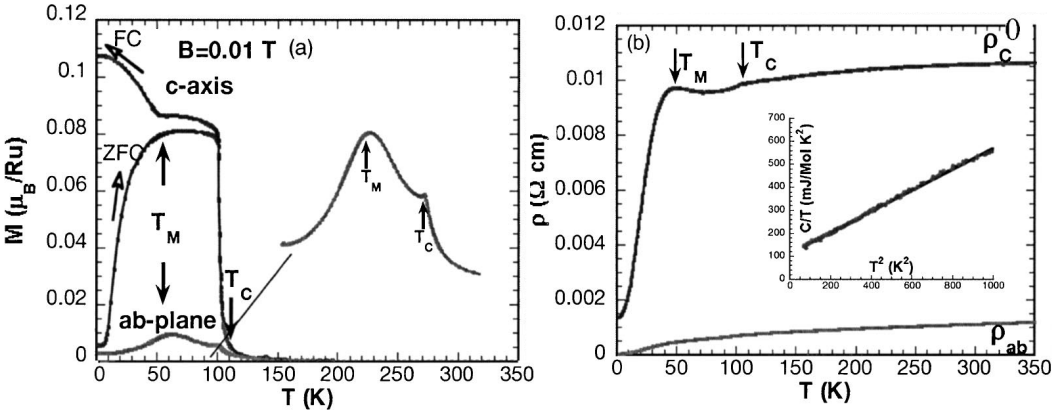


Figure 1.6: *(a): Magnetization curves of $Sr_4Ru_3O_{10}$ as a function of temperature. In the inset the zoomed behaviour for the ab plane. (b): Resistivities as a function of temperature. Both are from Ref.[22].*

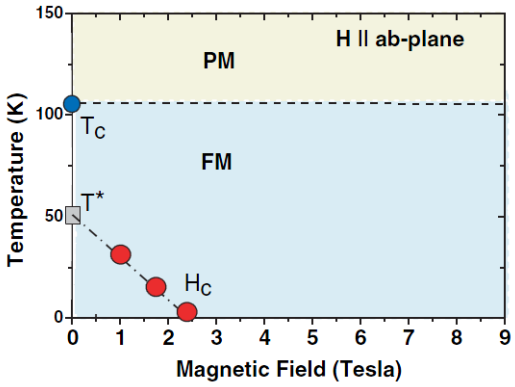


Figure 1.7: *The phase diagram of $Sr_4Ru_3O_{10}$, with the still unclear magnetic transition H_C, leading to a ferromagnetic (FM) behaviour up to the Curie temperature T_C [19].*

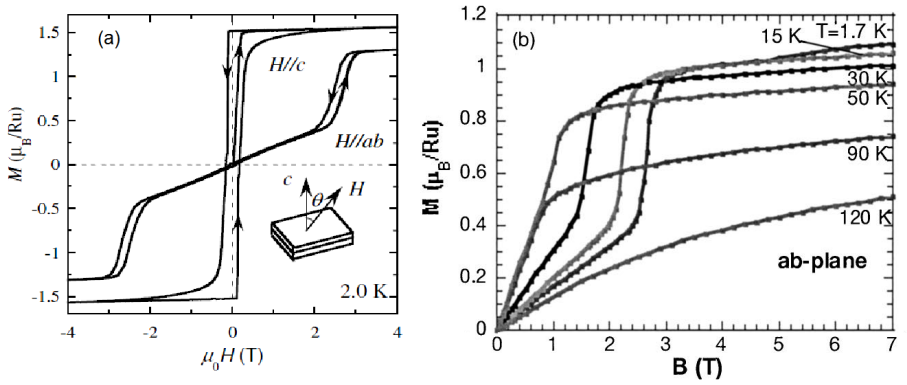


Figure 1.8: *(a): Isothermal magnetization as a function of B [20]. (b): Temperature dependence of the basal plane metamagnetic transition [22].*

Chapter 2

Theoretical models

In this chapter are described the main theoretical models used in the analysis of experimental data, and the physics behind the adopted experimental techniques.

2.1 Time-resolved Reflectivity: Two-temperature model

The non-equilibrium dynamic of the electron gas in a metal, irradiated by an ultra-short laser pulse, can be described using the so called two-temperature model (TTM).
In the initial equilibrium condition, the system has its global temperature; when a laser pulse impinges the sample's surface, some of the valence electrons absorb energy from the light, while the lattice remains cold. On a femtosecond time scale the hot electrons reach the equilibrium condition by electron-electron collisions, with a final temperature T_{el}. The hot electron gas then interacts with the lattice via electron-phonon ($e-ph$) scattering, and, after few tens of picoseconds, electrons and phonons are in thermal equilibrium, so the system has now a global temperature (T_{latt}) higher than the initial one.
The separation between the electronic and the lattice excitations, as described by the TTM, lies in the different time scale in which the Coulomb interaction among hot electrons and the $e-ph$ interaction occur.

The phenomenological model is then described by means of the following equations [23]:

$$\begin{cases} C_{el}(T_{el})\dfrac{T_{el}}{t} = I_{ext}(t) - G(T_{el} - T_{latt}) \\ C_{latt}(T_{latt})\dfrac{T_{latt}}{t} = G(T_{el} - T_{latt}) \end{cases} \tag{2.1}$$

where C_{el} and C_{latt} are the electronic and phononic specific heat, I_{ext} represents the external perturbation (i.e. the laser pulse), and G is the decay factor of T_{el} after the perturbation[1].It is worth noting that G is connected to the decay rate γ_{el-ph} :

$$G = \gamma_{el-ph} C_{el} \tag{2.2}$$

There is a link between γ_{el-ph} and the electron-phonon coupling constant λ (governing the energy exchange), that is been provided by Allen [23]:

$$\gamma_{el-ph} = \frac{3\hbar\lambda < \omega^2 >}{\pi K_B T_{el}} \tag{2.3}$$

where λ is defined by:

$$\lambda = 2 \int_0^\infty \frac{\alpha^2(\Omega) F(\Omega)}{\Omega} \, d\Omega. \tag{2.4}$$

In the latter formula, $\alpha^2(\Omega)F(\Omega)$ represents the phonons spectrum, approximated by an Einstein model: $F(\Omega) = \delta(\Omega - \Omega_0)$. By solving the TTM equations, we can describe the temperature decay time as:

$$\tau = \frac{\pi K_B T_{el}}{3\hbar\lambda < \omega^2 >}. \tag{2.5}$$

[1]The factor G is also the rise time governing lattice temperature's dynamics.

2.2 X-ray Magnetic Circular Dichroism (XMCD)

In general, X-ray absorption spectra of atoms in magnetic solids (or in solids in a magnetic environment), depend on three essential parameters: the sample orientation, the X-ray polarization, and the external magnetic field **B**[24].
When the spherical symmetry of an atom is broken due to a magnetic field, absorption spectra made with circularly-polarized (CP) light may depend on the helicity of the shined light, i.e. dichroism effect can occur. In this case, dichroism correspond to anisotropic contributions in XAS due to the non spherical spin density in the atomic volume, and we can define the XMCD spectrum as:

$$\Delta\mu \equiv \mu_+ - \mu_-, \tag{2.6}$$

where $\mu_+(\mu_-)$ is the XAS spectrum for the incident photon with $+(-)$ helicity. The same spectrum can be obtained with a single helicity, switching the direction of the external field B:

$$\Delta\mu = \mu_-(-\mathbf{B}) - \mu_-(\mathbf{B}) = \mu_+(\mathbf{B}) - \mu_+(-\mathbf{B}). \tag{2.7}$$

2.2.1 XMCD effect in $L_{2,3}$ edges

We can explain the dependence of XAS spectra on the polarization of the X-ray using a single-electron picture.
Let's think about a L-edge $(2p - 3d)$ X-ray absorption process, in which the valence states exhibit a Stoner splitting[2], and the impinging X-rays are composed of CP photons with angular momentum $q = \pm 1$ (in units of $\hbar$), collinear to the magnetization direction **M** of the sample. XMCD effect is then given by the difference in XAS intensity of the $p \to d$ transition

[2]By Stoner splitting we mean an energy separation between spin-polarized valence bands, i.e. a ferromagnet in which there exist spin states with a large number of electrons, and minor spin states with few electrons.[25]

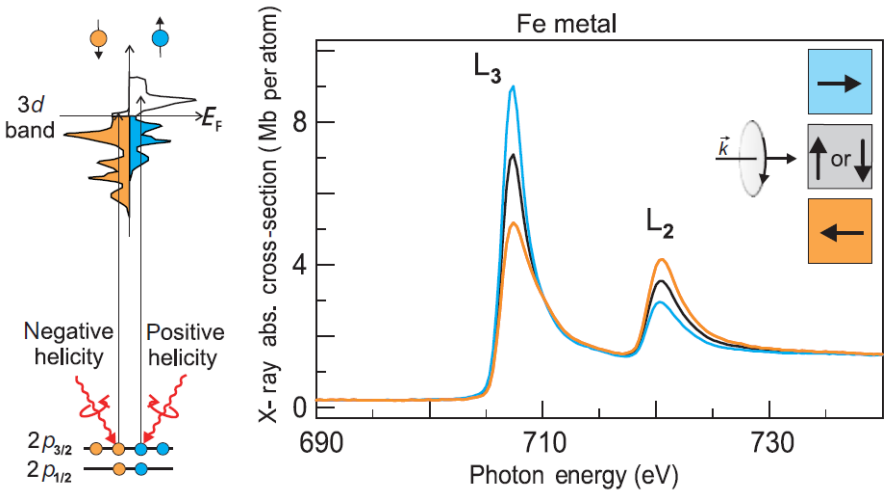


Figure 2.1: *Picture of the XMCD effect. From Ref.[25].*

occurring with positive and negative angular momenta of the photons, as illustrated in 2.1:

The quantum mechanical origin of dichroism can be understood using a simple atomic model, instead of a band one. We can think of a strong ferromagnet, where one of the two spin channel of d states is completely filled. For simplicity, we consider only the spin orbit splitting of the p states, and ignore the effect on the d electrons, so that the sample has only a spin magnetic moment, while the orbital magnetic moment is zero. It's then possible to write the $2p_{3/2}$ and $2p_{1/2}$ wave functions in the basis $|l = 1, m_l, s, m_s >$, and a linear combination of basis function $|l = 2, m_l, s, m_s >$ for the spin-up $3d$ wave function. Under the assumption of spin conservation, the angular part of the single transition intensity is given by:

$$\left| < d_n, \chi^+ | \frac{p_z^q}{r} | p_j, m_j > \right|^2 \tag{2.8}$$

where $n = 1 - 5$, $j = \frac{3}{2}, \frac{1}{2}$, $m_j = \pm\frac{3}{2}, \pm\frac{1}{2}$, $q = 0, \pm 1$, and χ^+ is the spin direction of the empty d states. The result is shown in the picture 2.2.

Signals coming from L_2 and L_3 edges are identical in magnitude but opposite in sign: this happens because at the L_3 edge X-rays with positive

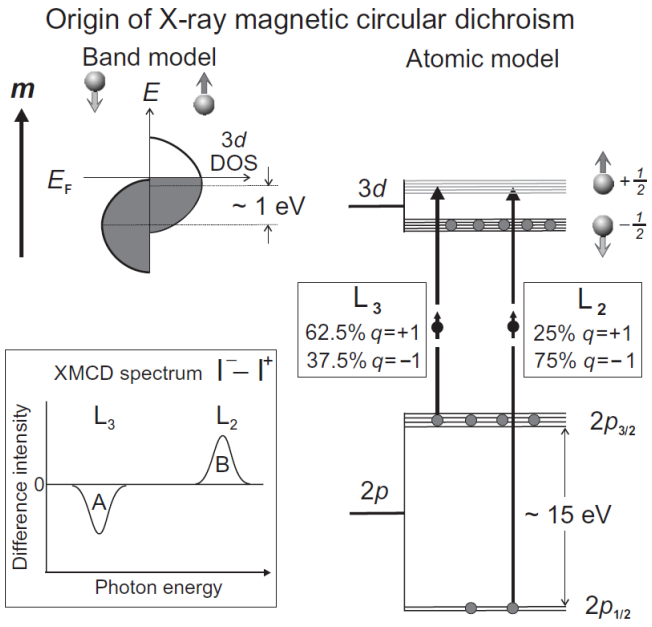


Figure 2.2: *Illustration of the L-edge X-ray absorption processes of circularly polarized photons. Comparison between a band model valence DOS with Stoner splitting (on the left) and an atomic model (on the right). Image taken from Ref.[25].*

photon spin excite more spin-up electrons than photons with negative spin. The opposite occurs for the L_2 edge.

2.2.2 Two step model

We can state a simple two-step model for the XMCD intensity. In the first step, the conservation of angular momentum during the X-ray absorption requires a transfer of momentum from the incident CP light to the excited electrons. Because electrons come from spin-orbit split states, the angular momentum of the photon couples in part through the spin via $j = l+s$, so the photoelectrons are spin polarized. This polarization is opposite for different photon spins, and also the $2p_{3/2}$ and $2p_{1/2}$ have opposite spin polarization due to their opposite spin-orbit coupling ($l + s$ and $l - s$ respectively).

In the second step, the unequal population of spin-up and spin-down of the valence shell acts as a detector for the spin of the excited photoelectrons. In order to have the best detection, the spin of the electrons has to be aligned

with that of the spin quantization axis of the empty states.

Finally, taking into account the two-times higher populations of the $2p_{3/2}$ state, one can find the intensity difference at the two edges. It is possible however to note that the pure photon spin configuration is not converted into a single-electron spin excitation, but some of the photon spin is converted into electron angular momentum, via the j coupling, and this is detected in the case that the valence shell has a nonzero orbital moment.

2.3 Resonant X-ray emission spectroscopy (RXES)

X-ray Emission Spectroscopy (XES) is an experimental technique involving second-order optical processes, in which a core electron is excited by an incident x-ray photon, and then the created core hole is filled by the decays of an electron, with the emission of an X-ray. If the core electron is resonantly excited to the absorption threshold, as in the XAS process, the resulting emission spectrum depends strongly on the incident photon energy: in this case we speak of resonant XES (RXES).

To see this, let us consider a scattering process in which an X-ray photon with frequency Ω and wave vector $\mathbf{k}_1$ is incident on a material, and as a result of the electron-photon interaction an X-ray photon with frequency ω and wave vector $\mathbf{k}_2$ is emitted. Taking into account the interaction up to the second-order perturbation term[3], the differential scattering cross section can be written as:

$$\frac{d^2\sigma}{d\Omega_{\mathbf{k}_2} d\hbar\omega} = \frac{(\hbar\omega)^2}{c^4}\left(\frac{1}{2\pi}\right)^3 W_{12}, \tag{2.9}$$

where $d\Omega_{\mathbf{k}_2}$ is the solid angle of the scattered light, and W_{12} is the transition rate, given by [26]:

$$\begin{aligned} W = \sum_j \frac{(2\pi)^2}{\hbar^2\omega\Omega}\left(\frac{e^2}{m}\right)^2 \delta(E_j - E_g + \hbar\omega - \hbar\Omega) \left| < j \left| \rho_{\mathbf{k}_1 - \mathbf{k}_2} \right| g > (\eta_1 \cdot \eta_2) \right. \\ + \frac{1}{m}\sum_i \left(\frac{< j \left| \mathbf{p}(\mathbf{k}_2)\cdot\eta_2 \right| i >< i \left| \mathbf{p}(-\mathbf{k}_1)\cdot\eta_1 \right| g >}{E_i - E_g - \hbar\Omega} \right. \\ \left. \left. + \frac{< j \left| \mathbf{p}(\mathbf{k}_1)\cdot\eta_1 \right| i >< i \left| \mathbf{p}(-\mathbf{k}_2)\cdot\eta_2 \right| g >}{E_i - E_g + \hbar\omega} \right) \right|^2 . \end{aligned} \tag{2.10}$$

Here, $|g>$, $|j>$ and $|i>$ are the initial, intermediate, and final states of the material system, with the corresponding energies E_g, E_j and E_i. η_1 and

[3]The lowest-order perturbation term has the form $\frac{e^2}{2mc^2}\sum_n A(\mathbf{r}_n)^2$, and the second-order term is $\frac{e^2}{2mc^2}\sum_n \mathbf{p}_n \cdot \mathbf{A}(\mathbf{r}_n)$, where $\mathbf{A}(\mathbf{r})$ is the X-ray vector potential.

η_2 are polarization directions of the incident and emitted photon; $\mathbf{p}(\mathbf{k})$ and $\rho_{\mathbf{k}}$are defined by:

$$\mathbf{p}(\mathbf{k}) = \sum_n \mathbf{p}_n e^{-i\mathbf{k}\cdot\mathbf{r}_n}, \tag{2.11}$$

$$\rho_{\mathbf{k}} = \sum_n e^{-i\mathbf{k}\cdot\mathbf{r}_n}. \tag{2.12}$$

We can use a schematic representation for the three terms in the square bracket, shown in figure 2.3. In particular, the first term is the elastic (Thompson) scattering, from the first order perturbation, while the second and the third term come from the second order. The denominator $E_i - E_g - \hbar\Omega$ assumes a crucial role in the case of RXES, because vanishes above the absorption threshold of the core electron, and we have to take into account the finite lifetime of the intermediate-state core hole, $\tau = \hbar/\Gamma_i$, into the value of the energy, in order to remove the divergence [4]. The RXES spectrum, then, depends strongly on the term:

$$F(\Omega,\omega) = \sum_j \left| \sum_i \frac{< j\,|T_2|\,i >< i\,|T_1|\,g >}{E_g + \hbar\Omega - E_i - i\Gamma_i} \right|^2, \tag{2.13}$$

where T represents the radiative transition between the considered states, and $T_i = \mathbf{p}(0)\cdot\eta_\mathbf{i}$, if we consider an optical dipole transition.

As can be seen from the expression 2.13, RXES is a coherent second-order process, which depends on both the incident and the emitted photon energies independently; so it's more useful than the Thompson scattering, which depends on Ω and ω only through $\Omega - \omega$. Therefore, we can obtain detailed informations about the electronic excitations tuning Ω to different electronic states i, that are different of each atomic species, so that the informations provided are atomic species dependent. Further, the RXES intensity is stronger than the Thompson's because of resonance effect.

[4] Γ_i represents the spectral broadening due to the core-hole lifetime in the intermediate state, as the sum of radiative and Auger contributions. It can be assumed as a constant, independent of the index i.

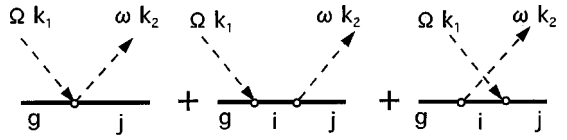


Figure 2.3: *Schematic representation of the three scattering terms of 2.10. Taken from [26].*

2.3.1 Connection between RXES and DOS of conduction band

Let's think of a RXES experiment in a metal, where a $1s$ core electron is excited virtually above the Fermi level (ε_F), and a $2p$ electron decays to the $1s$ state, emitting a photon. This radiative transition has an energy $\hbar\omega \simeq \hbar\Omega - (\varepsilon_F - \varepsilon_L)$, where $(\varepsilon_F - \varepsilon_L)$ is the binding energy of the $2p$ electron (see the scheme in 2.4). Disregarding electron-electron interactions, the RXES factor in 2.13 can be simplified as [26]:

$$F(\Omega,\omega) = \sum_{\mathbf{k}(k>k_F)} \left| \frac{1}{\hbar\Omega - \varepsilon_{\mathbf{k}} + \varepsilon_K - i\Gamma_K} \right|^2 \delta(\hbar\omega - \hbar\Omega + \varepsilon_{\mathbf{k}} - \varepsilon_L)$$

$$= \begin{cases} \frac{\rho}{(\Delta E_0^2 + \Gamma_K^2)} & \Delta E_0 \leq \Delta E_R \\ 0 & \Delta E_0 > \Delta E_R \end{cases}, \tag{2.14}$$

where

$$\Delta E_R = \hbar\Omega - (\varepsilon_F - \varepsilon_K)$$

$$\Delta E_0 = \hbar\omega - (\varepsilon_L - \varepsilon_K).$$

Here, Γ_K, ε_K, and ρ are, respectively, the lifetime broadening of the $1s$ electron, its core level energy, and the density of states (DOS) of the conduction band. We make use of ΔE_0 and ΔE_R because for $\Delta E_R < 0$ the peak of $F(\Omega,\omega)$ occurs at $\Delta E_0 = \Delta E_R$, while for $\Delta E_R > 0$ it occurs at $\Delta E_0 = 0$. So, with this example, we can see that there exist a direct

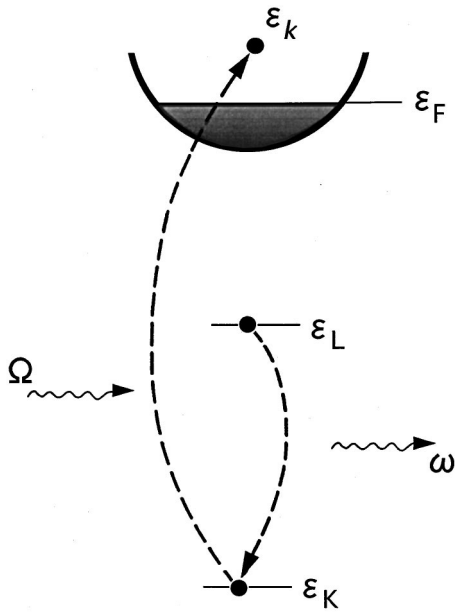


Figure 2.4: *Schematic representation of a 2p1s RXES in a metal. From Ref.[26].*

link between the DOS of the states below the Fermi energy and the RXES spectra. Moreover, the X-ray absorption spectrum (usually taken before an RXES experiment) can give information about the empty states. So we can eventually combine the two techniques to gain information about the valence and the conduction band.

Chapter 3

Experimental set-ups

3.1 Time-resolved Reflectivity

Time-resolved technique permits to study the non equilibrium optical properties of solids, like reflectivity and transmission, with temporal resolution. The used set-up allows to measure the variation of the reflectivity of the sample with sub-picosecond resolution. This is possible because laser pulses has femtosecond duration. The presence of the Optical parametric amplifier (OPA) permits to perform experiments over a broad wavelength range ($1200 - 2400\,nm$). In addiction, this technique has a high sensitivity, which means that it's possible to distinguish variations of signal on the order of 10^{-4}.

In experiments is measured the normalized variation of the reflectivity (ΔR) in time:

$$\Delta R(t) = \frac{R_{ex}(\tau) - R_{eq}}{c} \,, \tag{3.1}$$

where τ is the delay between the pump pulse and the probe (governed by the Scan Delay, see next section), R_{ex} is the reflectivity of the sample after the excitation of the pump, and R_{eq} is the reflectivity of the sample at equilibrium. Reflectivities are measured from the intensity of the probe beam reaching the photodiode. Behaviours at different temperatures can be studied thanks to a cryostat system, in which the sample is mounted.

3.1.1 Experimental set-up

The laser source in our set-up consist of:

- Coherent Verdi V-18 laser
- Coherent Mira Seed laser
- Coherent Stretcher/Compressor
- Coherent RegA 9050
- Coherent OPA 9850

Coherent Verdi V-18 is a solid-state diode-pumped $Nd:YVO_4$ laser, which generates a continuum monochromatic ($532\,nm$) output through a frequency doubling non linear crystal (called LBO). The output power is $18\,W$. The green light is used as an optical pump for both the Mira Seed and the RegA. The former is a Ti:Sapphire (Al_2O_3 doped with Ti_2O_3) mode-locked laser, whose exit pulse is tunable from 760 to $840\,nm$, and at the wavelength of $800\,nm$ has about $30\,nm$ of bandwidth and $120\,fs$ of duration, at a repetition rate of $76\,MHz$. The Stretcher/Compressor is a device capable of stretching in time the pulse from the Mira Seed with a set of gratings and lenses. This stretched pulse passes to RegA, and eventually it's re-compressed by a second pass in the Stretcher/Compressor. At the end of this stage, the laser has a $50\,fs$ duration per pulse and a peak power of $\sim 20GW/cm^2$.

Between the stretching and compression operations, the beam goes inside a regenerative amplifier system (RegA). This system uses the pump source coming from the Verdi laser to produce a $250\,kHz$ tunable output, amplifying the stretched pulse from the Mira Seed to the μJ level (which means over thousand times).

After the final compression stage, the beam goes into the OPA. This device is a wavelength converter that turns the RegA output into amplified femtosecond pulses, ranging from 1200 to $1600\,nm$ (OPA signal) at $250\,kHz$.

At the same time paired pulses with tunable wavelength, longer than the signal pulses (from 1600 to 2400 nm) are generated (OPA idler).

It is possible to follow the optical path of the laser beam, looking at the sketch in figure 3.1. At the end of the laser system, the light pulses have a repetition rate of 250 kHz and output power of $\sim 1.2\,W$. The beam produced by the laser is split by a beam-splitter 70−30 into two beams: the pump beam (called also the "pump", here after) with 70% of the original power, and the probe beam (called the "probe") with 30% of the previous power. The former beam passes through a Scan Delay, which is a motorized device containing a retro-reflecting mirror, placed on a sledge, that permits to change the optical path length of the pump. This beam is then reflected into an attenuator (made of a software-rotatable half-wave plate and two mirrors placed at the Brewster angle). This device permits to automatic adjust the intensity of the pump beam, in order to perform measurements at various fluences[1]. After the attenuator, the pump beam passes through a chopper and it's finally focused on the sample by a lens ($L1$ in figure).

The probe beam instead, after passing through the beam splitter, goes into the OPA, and exits with a tunable wavelength ($1200 - 2400\,nm$), which can also be selected using a polarizer, placed after the exit window. The beam is then attenuated by a filter before being focused on the sample by a spherical mirror ($SM1$). The probe intensity must be limited to few tens of $\mu J/cm^2$ in order to avoid strong excitation of the system, so the best filter was chosen each time to preserve this condition and, on the other hand, to keep a good signal. Spatial coincidence of the two beams on the sample surface requires also that the spot of the probe must lie inside that of the pump (diameters were typically 30 μm and 90 μm respectively),while the temporal coincidence of the two beams impinging on the sample must be obtained imposing an equal optical path.

The probe, reflected by the sample, is collected by a lens ($L2$) and focused on a photodiode. In order to avoid spurious signal coming from the reflection of the pump, we used the two beams with orthogonal polarization, and a

[1]The fluence is defined as the energy released by a laser pulse per surface area: $F = E_P/A$, where $A = \pi r^2$ if we consider a round spot.

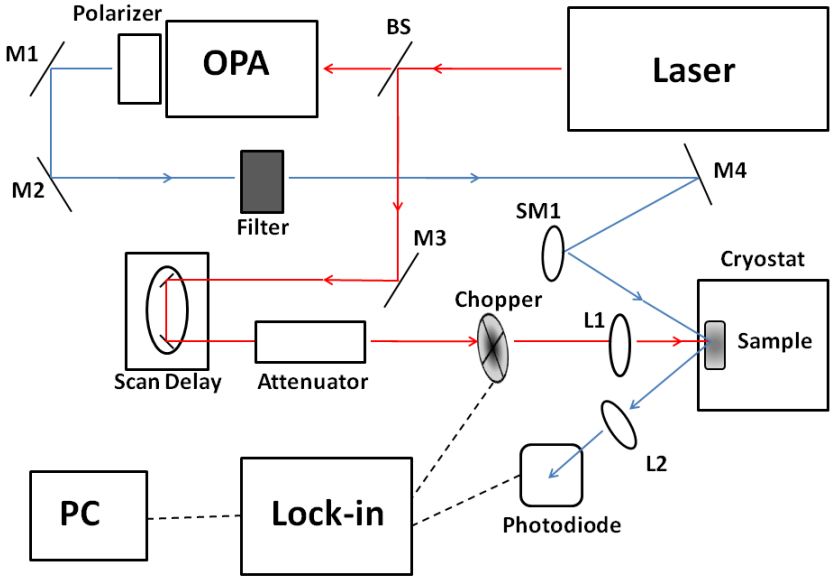


Figure 3.1: *Time-resolved Reflectivity experimental set-up.*

polarizer was placed before the photodiode. In particular, the pump beam was s-polarized, thanks to the Brewster mirrors placed after the attenuator, while the probe was p-polarized. The signals coming from the photodiode and from the chopper are collected by a lock-in amplifier, which acquires only the component of the reflected signal in phase with the chopper rotation and at its reference frequency, $13kHz$, avoiding noises related to other frequencies. This signal is then recollected in the computer, while the reference reflectivity is instead collected directly from the photodiode. The length of a scan is instead correlated to the temporal duration of the Scan Delay oscillation, also called the rise time (around $0.2s$ for a $10ps$ delay). The number of points of each scan, corresponding to the resolution of measurements, is then given by the ratio between the rise time and the integration time of the lock-in (around $1ms$).

The sample is mounted inside a vacuum chamber ($\sim 7 \cdot 10^7 mbar$), and a helium transfer refrigerator system (cryostat) is placed on the top of the manipulator. Cooling is accomplished by the controlled transfer of liquid helium through a hollow heat exchanger, adjacent to the sample interface.

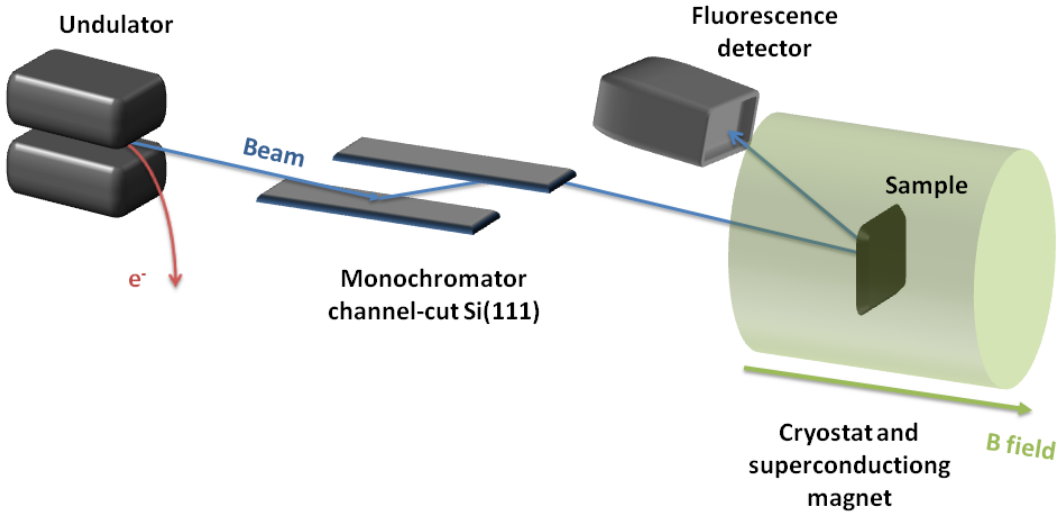


Figure 3.2: *Schematic representation of the ID12 beamline at ESRF.*

3.2 XMCD

3.2.1 Set-up

Magnetization measurements were carried out at the beamline ID12 at the European Synchrotron Radiation Facility (ESRF)[27], dedicated to polarization-dependent X-ray absorption studies. The beamline source is a helical undulator, with flexible polarization (left/right CP), and a $Si(111)$ double crystal monochromator. After this device, the polarization rate[2] drops to $\sim 4\%$ at the Ru L_2 edge and $< 1\%$ at the L_3edge, because the vertical part of the polarized light is strongly absorbed by the Si gratings geometry, at these particular energies.

The experimental vacuum chamber consists of a cryostat (capable to reach $4\,K$ under liquid helium cooling) and of a superconductor magnet, which was able to produce a uniform magnetic field around the sample, with a maximum intensity of $7\,T$. The incident beam direction is always parallel to the applied magnetic field direction (see figure 3.3). X-ray absorption spectra were recorded from the fluorescence yield (FY) by means of a multi-element

[2]Polarization rate is defined as the rate between the amplitudes of the primary axes electric field.

fluorescence detector[28], placed in front of the sample. The sample holder can be rotated along the horizontal axis and lifted with respect to the incident beam direction. XMCD signals were recorded by flipping the circular polarization at each energy point with a single value of the external magnetic B field, and then with the same field value in the opposite direction, in order to avoid any spurious residual XMCD signal [25]. So the XMCD spectrum is obtained from each absorption cross section σ by following

$$\sigma_{XMCD} = \frac{\sigma_{-}^{\uparrow} + \sigma_{+}^{\downarrow}}{2} - \frac{\sigma_{+}^{\uparrow} + \sigma_{-}^{\downarrow}}{2}, \tag{3.2}$$

where the arrow stays for the type of CP light (e.g. $\uparrow$ for right-CP and $\downarrow$ for left-CP), and the $+/-$ for the direction of the B field with respect to the momentum of the incident photons. By setting the monochromator at fixed energy, corresponding to a large XMCD signal, one can also record a Ru-specific magnetization curve by sweeping the B field.
Since B was always parallel to the direction of incident photon beam in a fixed configuration, the $Sr_4Ru_3O_{10}$ single crystals were mounted on the sample holder in order to apply the magnetic field along either the ab-plane (configuration A) or the c-axis (configuration B), as sketched in figure 3.3.

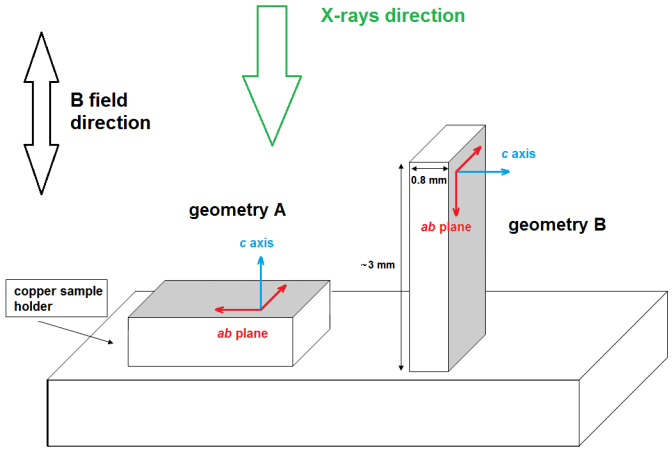


Figure 3.3: *Sketch of the mounting of the two samples used in the XMCD experiment.*

3.3 RXES

3.3.1 Experimental set-up

The RXES experiment was performed at the beamline for advanced dichroism (BACH) of the Elettra synchrotron laboratory in Trieste. The experimental geometry is shown in figure 3.4. RXES spectra can be acquired with a ComIXS fluorescence spectrometer[29], equipped with two variable-line-spacing spherical gratings, and a charge-coupled device (CCD) with $20 \times 20 \mu m^2$ pixel. The spectrometer is located in the horizontal plane with a take-off angle of 60° with respect to the incident beam direction. The electric field E_{inc} of the incident beam could be set either horizontal or vertical, with respect to the experimental geometry.

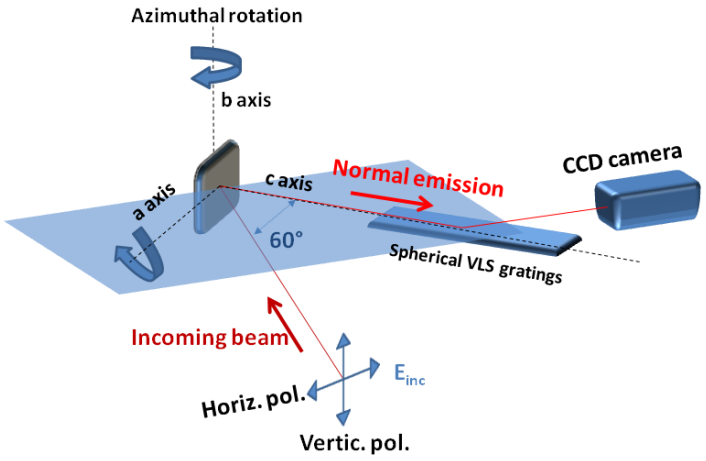


Figure 3.4: *Experimental geometry of the BACH beamline.*

The sample is located inside a ultra-high vacuum (UHV) chamber on a sample holder, and it could be rotated around the horizontal axis, perpendicular to the surface, and along the vertical axis, in the sample surface plane. The crystalline ab plane always lied parallel to the sample holder, while the c axis is normal to the surface. In our set-up configuration, in the linear vertical polarization E_{inc} lied completely in the ab plane, while for linear

horizontal polarization E_{inc} was 30° off the normal.

The sample was cleaved *in situ* along the *ab* plane, in UHV condition. X-ray absorption spectra were taken in total electron yield mode[25] before each set of RXES measurements, with a resolution better than $0.2\,eV$. The emission spectra were recorded in normal emission, using the second order of diffraction, and the acquisition time was 30 min per spectrum.

Chapter 4

Data analysis and discussion of results

4.1 Time-resolved reflectivity

4.1.1 Description of the data

Time-resolved reflectivity measurements on $Sr_3Ru_2O_7$ were acquired in the infrared region of the spectrum ($1200 - 2400\,nm$), using the frequency tunability of the OPA (section 3.1.1). We performed a scan changing the wavelength of the probe at two different temperatures, $15\,K$ and $50\,K$, i.e. below and above the FL-NFL transition (see section 1.2.2). We then made use of two different probe frequencies, $1300\,nm$ and $2200\,nm$ (its idler), to scan the change of reflectivity in a temperature range from $15\,K$ to $350\,K$. The pump beam fluence for these measurements was fixed at the 25% of its maximum value, in order to have the best signal to noise ratio, avoiding at the same time any possible sample damage.
Each experimental spectrum is an average of $250 - 500$ scans, depending on the signal to noise ratio. The scan range of the Scan Delay was set to $20\,ps$ for the first data set at fixed temperature, and to $10\,ps$ for the data set at fixed wavelength. The acquisition time was $5 - 10$ min per each spectrum, depending on the available signal.
Figure 4.1 shows the behaviour of the differential reflectivity as a function

of the probe wavelength. Here, the gap around $1600\,nm$ is due to the lack of signal at these frequencies. The value of the differential reflectivity, for a particular time delay of $15\,ps$ between the pump and the probe pulses, are reported in figure 4.2.

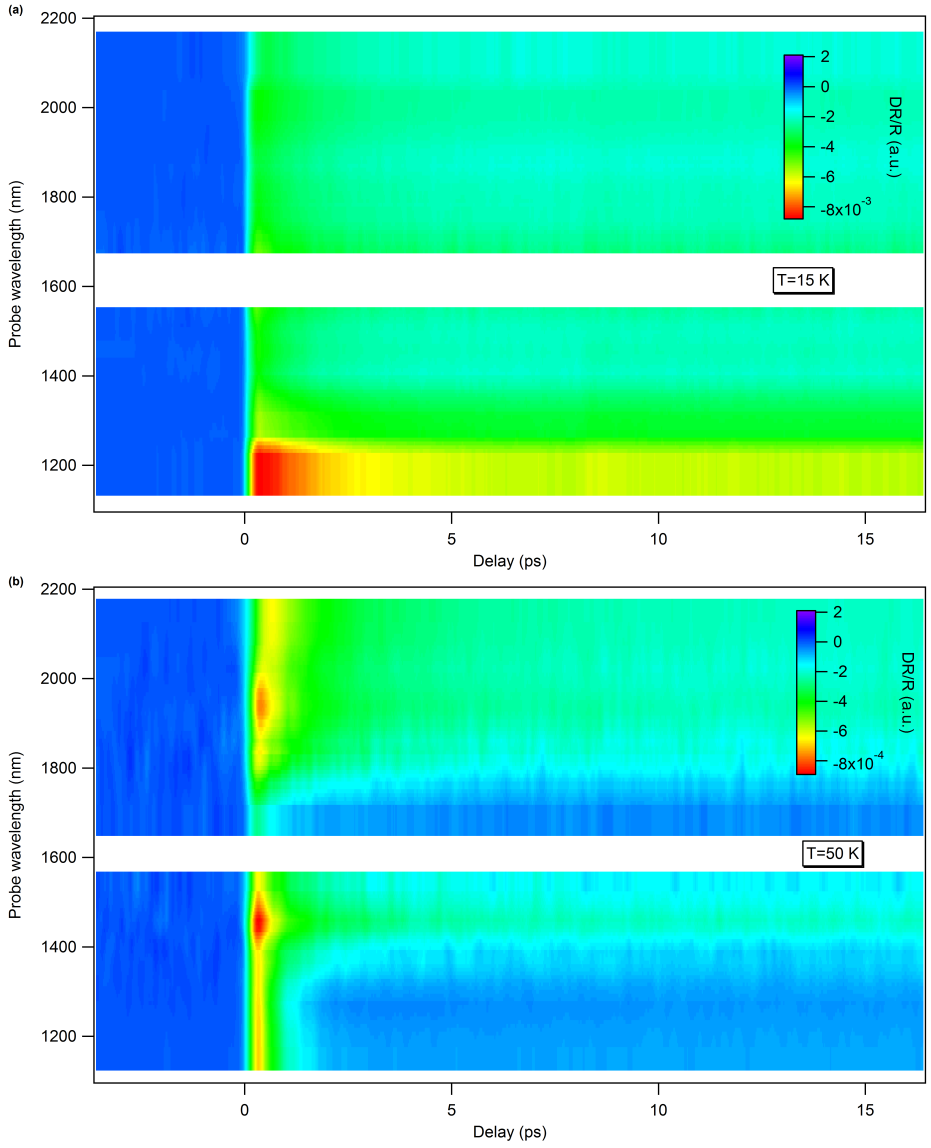


Figure 4.1: *Image plots for the time-resolved reflectivity data taken at different probe wavelengths. In (a) the data at $T = 15\,K$, in (b) the data at $T = 50\,K$.*

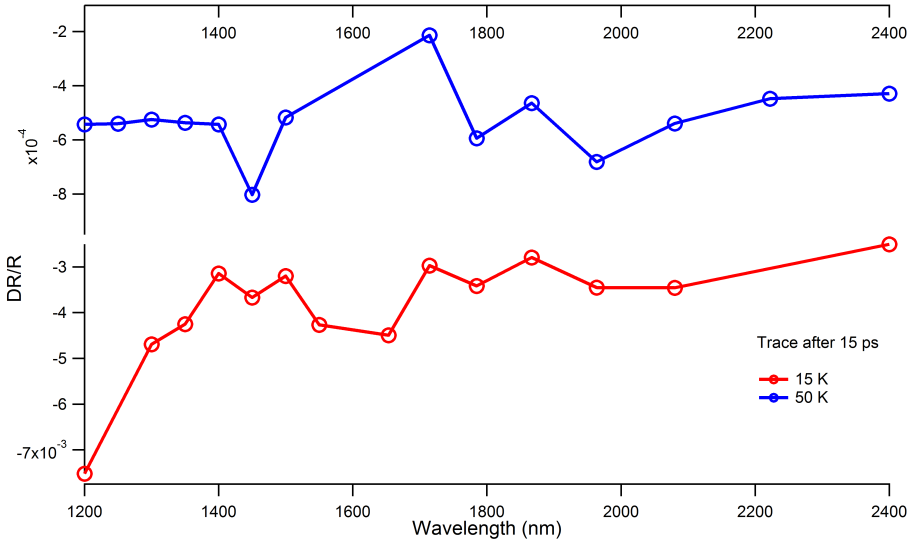


Figure 4.2: *The value of the reflectivity after a time delay of* $15\,ps$ *between the pump and the probe pulse, for the data set at* $15\,K$*, in red, and for the data at* $50\,K$*, in blue.*

We report an example of the raw data in figure 4.3: the 3D surface plot in 4.3(a) shows the differential reflectivity (DR/R) as a function of the delay between the pump and the probe. Different data are plotted as a function of the temperature. The image in 4.3(b) represents the thermal evolution of the low temperature data set (different colors are used to describe the intensity of the reflectivity).

Data was initially fitted by using the method reported in section 2.1. In figure 4.4(a) we report two reflectivity data (rescaled, for a best vision), taken at $16.3\,K$ and at $151\,K$, togheter with the best fitting curve, which made use of a single exponential decay. A test on the goodness of a single decay fitting procedure is shown in figure 4.4(b) (see the discussion in the next section).

The low temperature results are displayed in figure 4.5, wherethe scattering rate as a function of the temperature is reported for the two probe wavelengths.

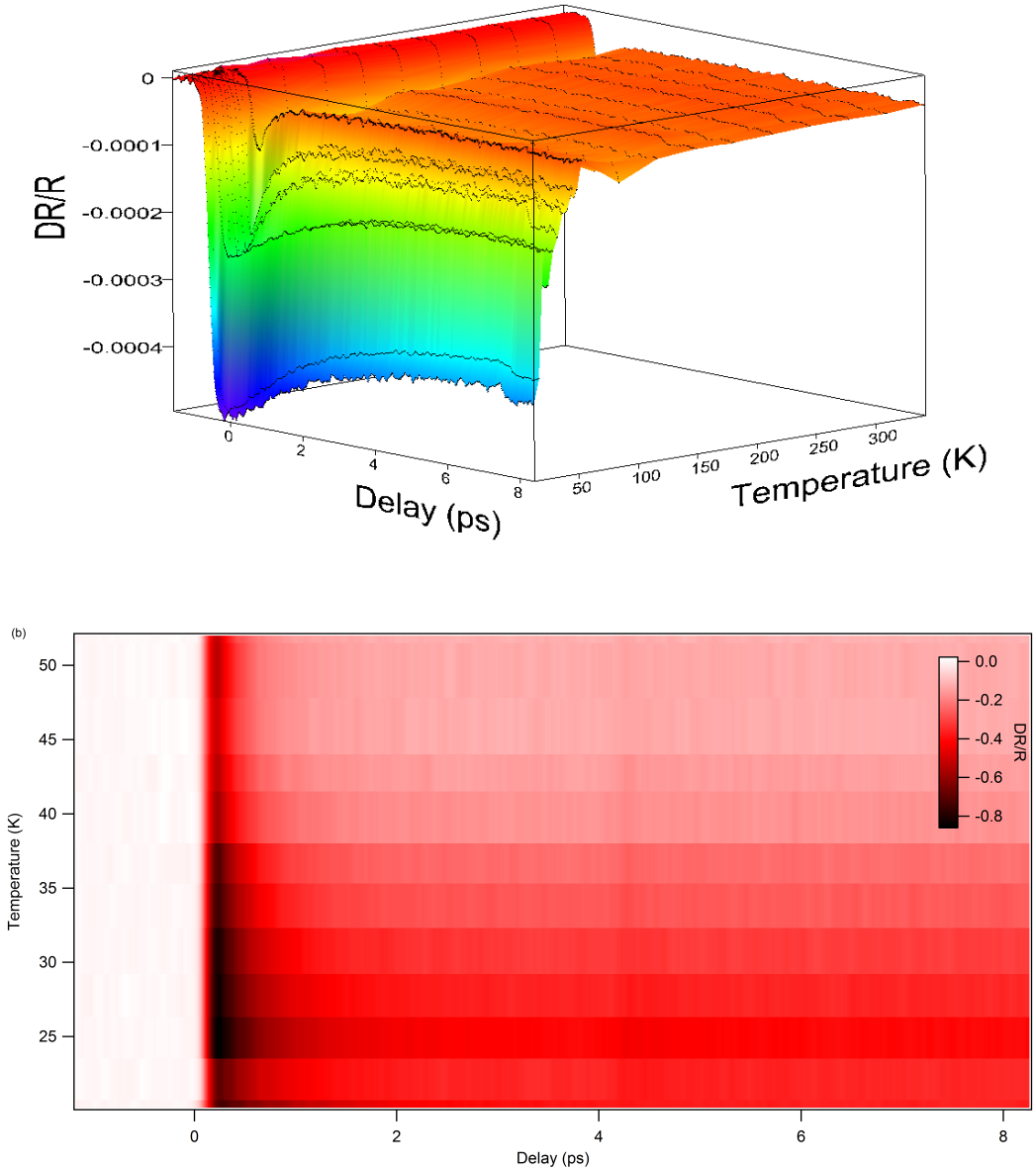


Figure 4.3: *Example of data evolution at different temperatures. In (a) the differential reflectivity as a function of the delay between the laser pulses and the temperature. In (b) the thermal trend of the low temperature spectra.*

Figure 4.6 and 4.7 shows, respectively, the slow and fast decay rates, which were extracted from the fitting analysis performed by means of a two exponential decay fit (the model is described in the appendix). The data sets used is the same of the previous fitting analysis.
The last figure (4.8) represents the evolution of the offset parameter for the two probe wavelengths.
Each point of the parameters coming from a fitting procedure is affected by a statistical error which lies inside the round dots used in the plot. The degree of reproducibility of our data was not tested with sufficient accuracy to state a correct sistematic error bar.

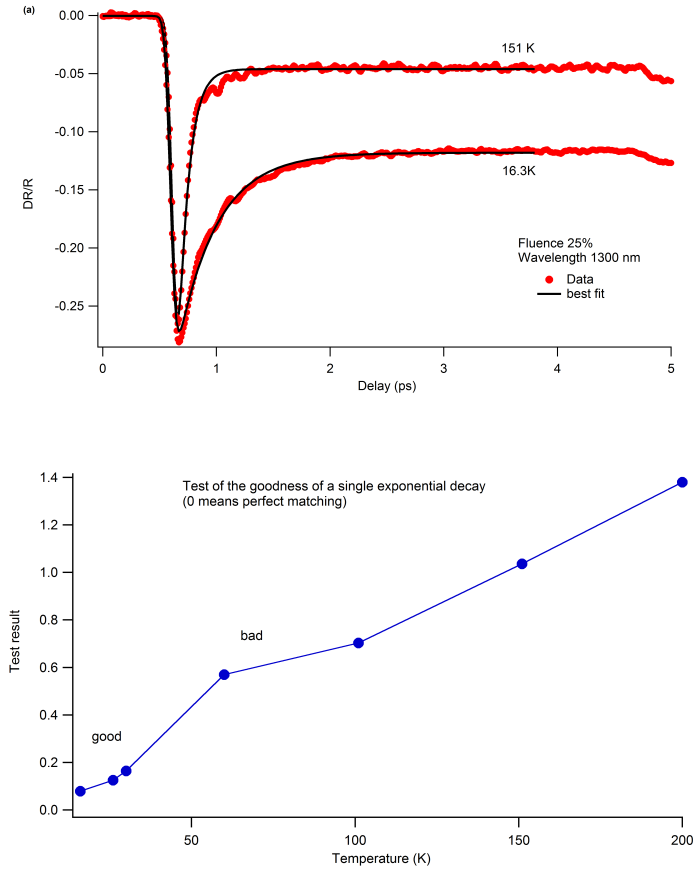


Figure 4.4: *In (a): comparison between fits with a single exponential decay, for two different temperature. Data are not in scale. In (b): a test to evaluate the goodness of a single exponential decay.*

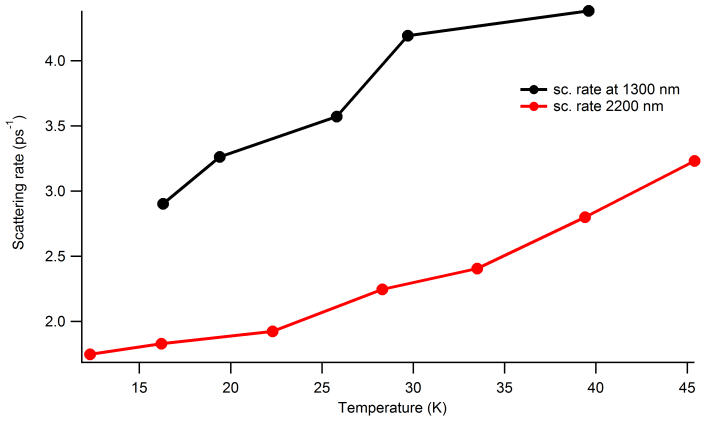


Figure 4.5: *The evolution in temperature of the scattering rate, for measurements taken at* 1300 *nm (in black) and at* 2200 *nm (in red) probe wavelengths, at* 25% *pump fluence.*

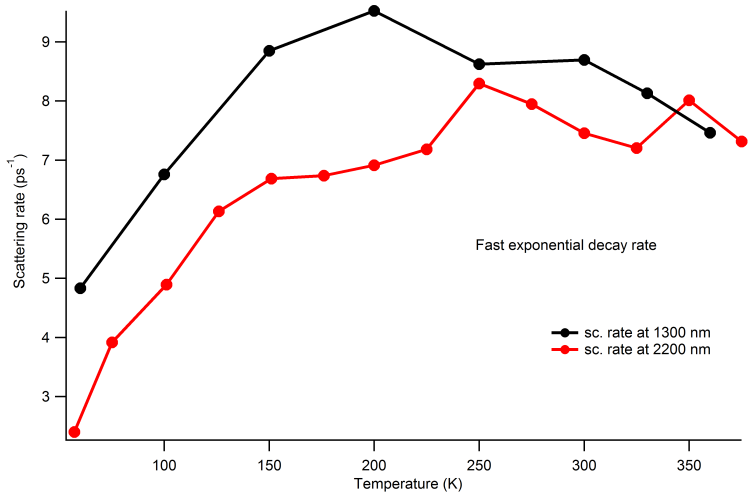


Figure 4.6: *Thermal evolution of the fast scattering rate, in a two decay fitting procedure, reported for two different probe frequencies.*

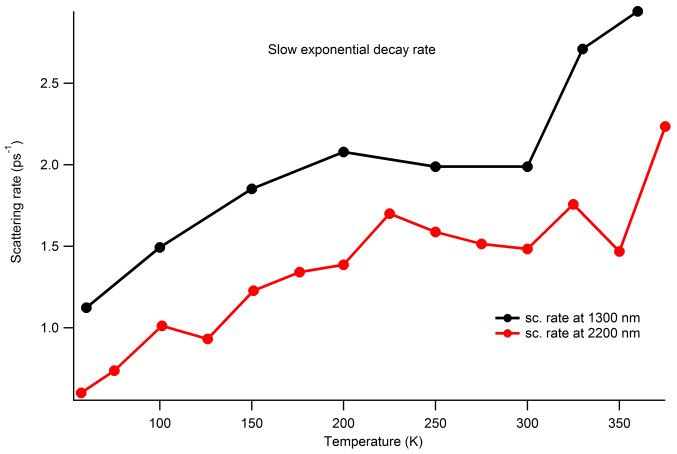


Figure 4.7: *Thermal evolution of the slow scattering rate, in a two decay fitting procedure, reported for two different probe frequencies.*

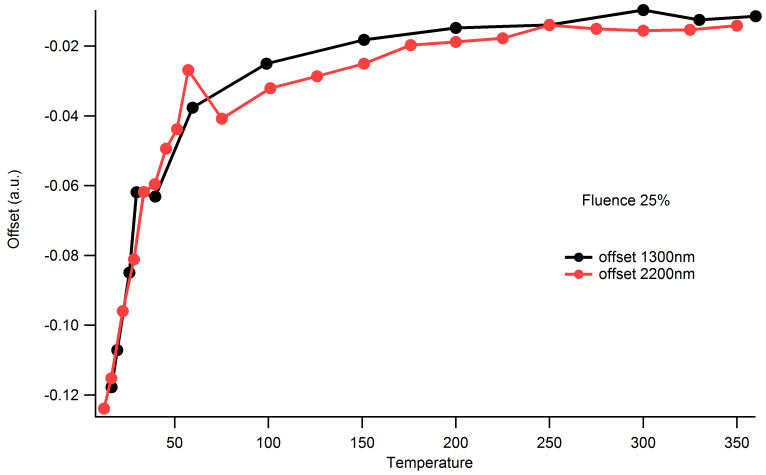


Figure 4.8: *Thermal evolution of the offset parameter, for the two probe frequencies.*

4.1.2 Data analysis and discussion

Figure 4.1 shows that the response of the reflectivity of $Sr_3Ru_2O_7$ at different probing wavelength is different above and below the FL-NFL transition. In particular, there is a pronounced change in the reflectivity for the $15\,K$ data around $1200\,nm$. The offset at a time delay of $15\,ps$, reported in figure 4.2, shows an enhancement in the $15\,K$ data toward high frequencies, while the

$50\,K$ data seem to have a flat trend. Thus, the response at different frequencies of the compound seems to be different above and below the FL-NFL transition. Further measurements are needed to investigate the response in the spectral visible range, in order to confirm the presence of a real, and very peculiar, trend.

Figure 4.4(a) shows that a single exponential decay manage to fit well the data at low temperature, but is not able to reproduce correctly the data at high temperature. To prove the goodness of the single exponential decay fitting function, we performed a test comparing the difference between the value of the single decay fitting function and the data. In figure 4.4(b) we report the sum of the absolute discrepancy between the data and the fit, normalized by the data magnitude, and calculated in the energy range $[0.7 - 3]\ ps$, i.e. after the main peak in the reflectivity[1]. The test showed that low temperature data are well described by a single exponential decay , where only a low discrepancy between the experimental data and the fit is present. The goodness of a single exponential fit procedure, however, get worst due to the transition between the FL and the NFL regime. These facts could indicate that in the FL regime a simple exponential decay mechanism can be used to reproduce the trend of the reflectivity, as in the case of a simple metal[30], while in the NFL regime the disexcitation mechanism changes, and new scattering channels are present. We then decided to analyze the data using a single exponential decay for the low temperature region (till $\sim 50\,K$), and a double exponential decay for the data at the remaining temperatures.

The decay rates in the low temperature range (figure 4.5) display an approximately linear trend. In particular, we can see only an offset between the data at the two different probe wavelengths. The fast exponential decay in figure 4.6 shows two distinct thermal behaviours: a first increasing, for $T < 150\,K$, and a second trend, almost flat, above $150\,K$. The behaviour of the slow scattering rates is instead different, and presents a growth above $200\,K$, vis-

[1]The value reported in figure 4.4(b) is then described as $\sum_{0.7-3}\left[\frac{f-d}{d}\right]^2$,where f and d correspond respectively to the point of the fit and the data at the particular time interval considered.

ible especially at 2200 nm. The dynamics for the two studied wavelength, also in this case, are shifted in values, and the rate at 1300 nm is faster than that at 2200 nm.

A similar behaviour on the thermal trend of the scattering rate was in part found with static reflectivity measurements by Mirri and coworkers[31], whose results are shown in figure 4.9. Here, the main plot reports the free electron relaxation rate Γ as a function of the temperature T. The relaxation rate has been obtained from a conventional Drude fit, from static reflectivity measurements. We can see that a clear change in the linear trend of the relaxation rate is present between 200 K and 300 K, which has been imputed to a structural transition, and a less evident change in the trend is expected under 50 K.

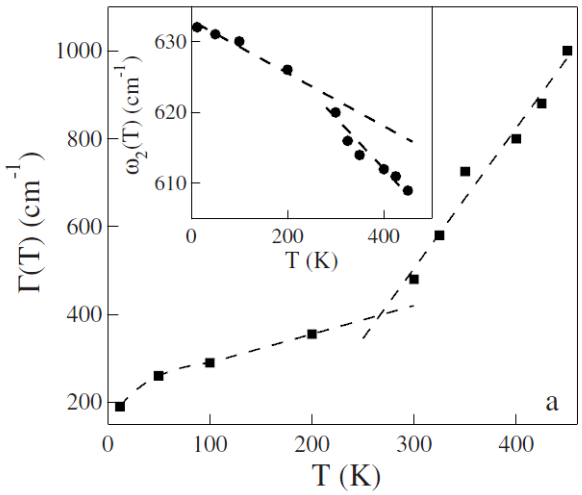


Figure 4.9: *Evolution in temperature of the free electron relaxation rate (Γ), obtained from a conventional Drude fit on static reflectivity data. In the inset, the frequency of an in-plane stretching mode versus the temperature, showing a structural transition between* 200 *and* 300 K. *Image taken from Ref.[31].*

The trends of the offset parameter of figure 4.8 are similar for the two studied frequencies, and present a (almost) linear thermal increasing up to $\sim 40\,K$, followed by a transition region, and a slow increasing at temperatures above 100 K. The linear trend of the first points of the offset corresponds to the FL temperature range, while the transient region marks the crossover

between a FL and NFL behaviour, as already shown in figure 1.4. The offset is not affected by the transition occurring around $250\,K$.
The fact that only the slow decay mechanism manage to see the high temperature transition could indicate that the scattering processes involves different coupling between electrons and bosons. The lattice properties affected by the transition, whose behaviour enters in the second (slower) decay, are not involved in the fast decay mechanism. At the present stage we can't state a correct physical interpretation for the two scattering rates, in terms of a well defined three temperature model (described in the appendix). For this reason, more studies are needed in order to understand correctly our last data.

4.2 XMCD

4.2.1 Data analysis

The magnetic properties of the $Sr_4Ru_3O_{10}$ compound were studied by carrying out XMCD measurements at the Ru $L_{2,3}$ absorption edges ($2p-4d$ dipole transition, $2.8-3.0\,keV$), using the set-up configuration described in section 3.2.1. In particular, the magnetization curves were recorded by measuring the dependence of the dichroic signal at the Ru L_2 absorption threshold as a function of the applied magnetic field and of the temperature. As a result of the quantitative analysis of these data, few points of the phase diagram across the FM and the metamagnetic transitions were reconstructed.
In figure 4.10 we present the mean value of the XMCD intensity, for the Ru $L_{2,3}$ absorption edges, and of the data residual[2], taken in configuration A. Here, the external magnetic field **B** was almost parallel to the c axis, and so was the direction of the incoming photons. B was set at $2\,T$ and the sample was cooled down to $4\,K$. In figure 4.10(a) is reported the XMCD signal at the L_2 edge ($\sim 2.97\,keV$) after a 32 scans iteration, while in figure 4.10(b) we show the XMCD signal at the L_3 edge, after a longer 60 scan iteration.

[2]Residual is defined as the half value of the difference between the XMCD intensity calculated with a particular B field value, and that with the same B in the opposite direction. If the final XMCD intensity is comparable with its residual, the measure cannot be considered good.

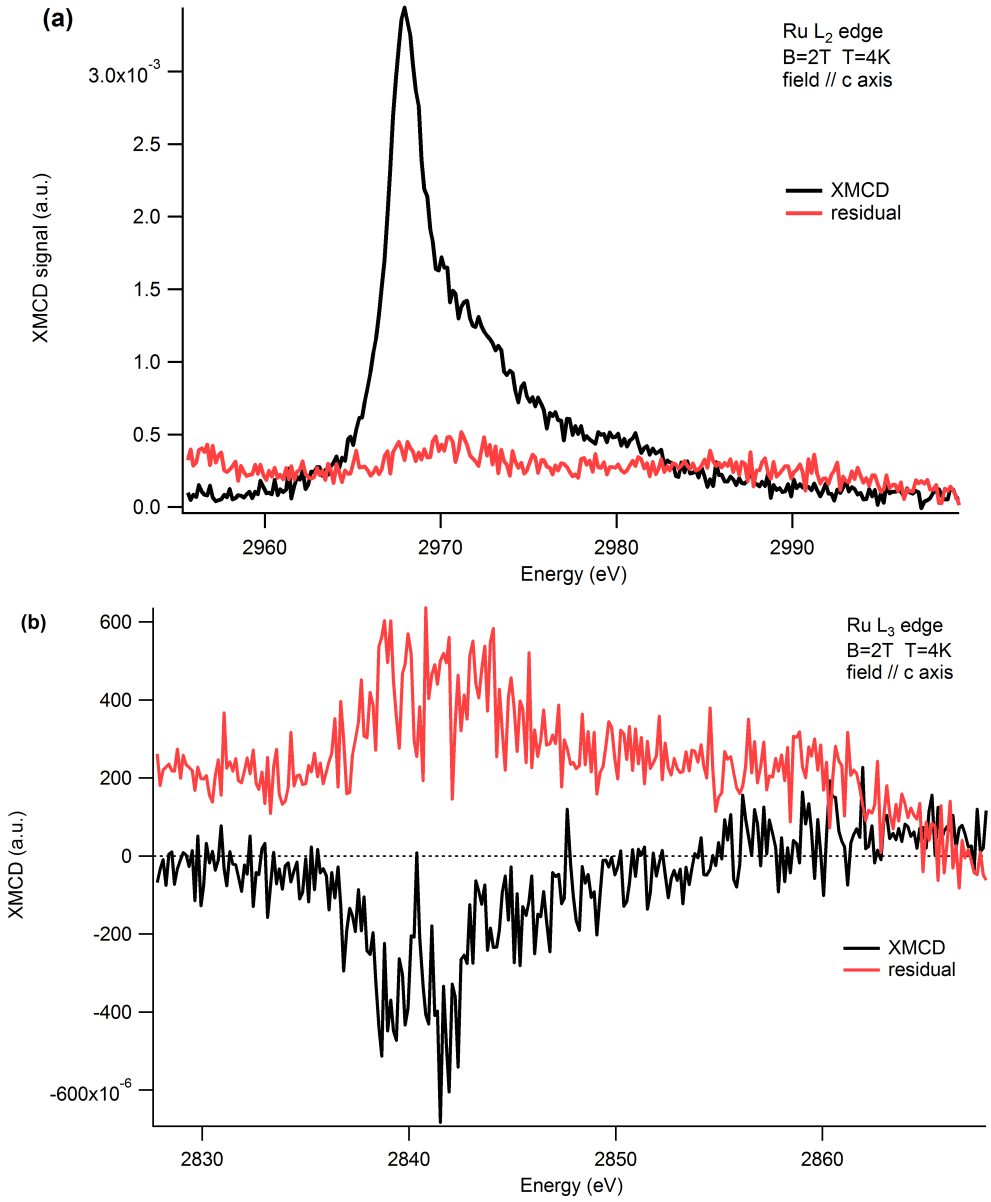


Figure 4.10: *XMCD signals of Ru L_2 edge (up), after 32 scans iteration, and L_3 (down) edge, after 60 scans, with the corresponding residual in red.*

The magnetization curve data, for $\mathbf{B}//\hat{\mathbf{c}}$ (configuration A), are reported in figure 4.11. The spectrum has been taken fixing the beam energy at the value corresponding to the maximum XMCD signal on L_2 (around $2968\,eV$), and sweeping the B field from $-2\,T$ to $2\,T$ (saturation values) and *vice-versa*. In figure 4.12 are displayed the magnetization curves performed by rotating the sample by $\vartheta = 75°$ with respect to the $\hat{\mathbf{c}}$ axis. In this configuration, the projections of the magnetic field along $\hat{\mathbf{c}}$ and on the ab plane were $B\cos\vartheta$ and $B\sin\vartheta$ respectively. The red curve shows the spectrum performed with the sample cooled to $20K$, for a B intensity ranging from $-4\,T$ to $4\,T$, while in the inset is reported, in black, the similar behaviour for the sample cooled down to $4K$.
The magnetization curve at $T = 4\,K$, for the sample in configuration B (i.e. with the magnetic field pointing along the sample ab plane), is reported in figure 4.13. The gray and black curves are here used to distinguish the sweep direction of the of B, represented by the arrows. In the inset are plotted the difference between the black curve and the gray curve, in red, and the integral of the difference curve, in blue.
Several magnetization curves, for different temperatures ($4\,K$, $20\,K$, $40\,K$ and $60\,K$), are reported using different colors in figure 4.14, for $B = 4\,T$ directed along the ab plane.

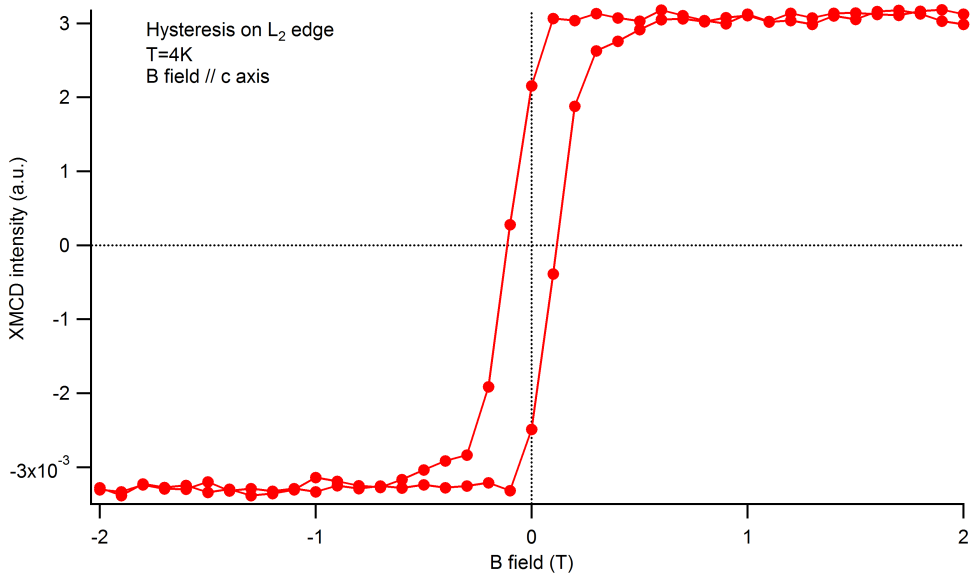


Figure 4.11: *Hysteresis cycle on the L_2 edge, with* **B** *applied parallel to the c axis.*

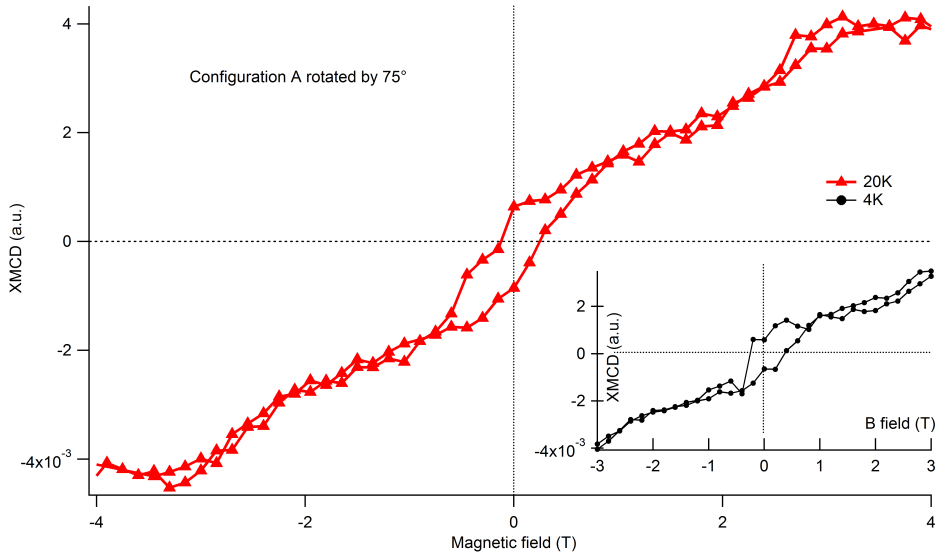


Figure 4.12: *Hysteresis on configuration A rotated by 75° around the c axis.*

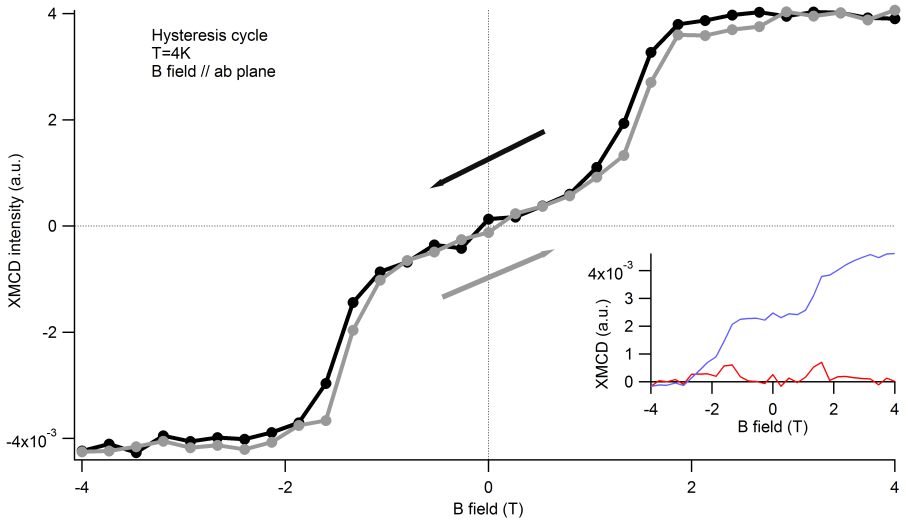


Figure 4.13: *Magnetization curve taken at the L_2 edge, with* **B** *applied parallel to the ab axis. In the inset: in red the difference between the black curve and the gray curve; in blue the integral of the difference curve. The blue curve has two increasing parts, corresponding to hysteresis present in the metamagnetic transitions.*

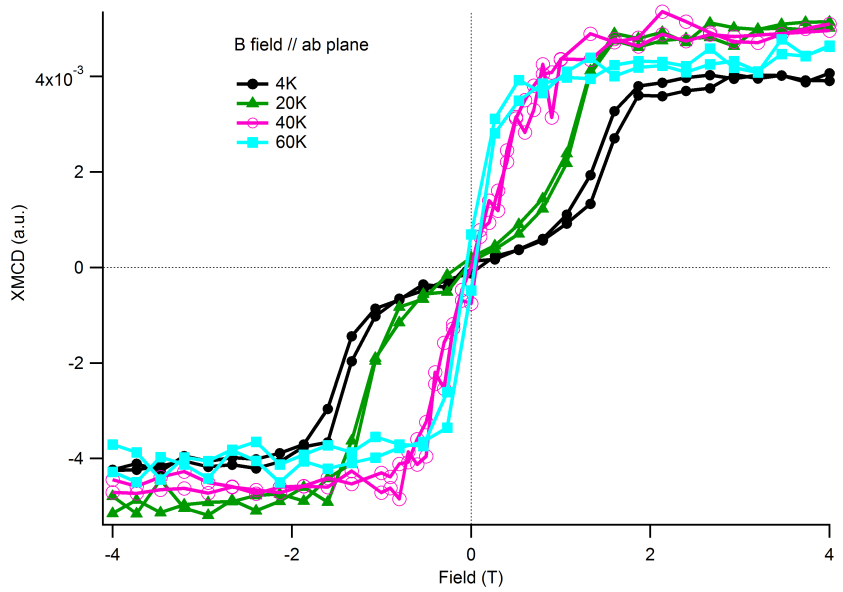


Figure 4.14: *Magnetization curves at different temperatures, with* **B** *parallel to the ab plane.*

4.2.2 Discussion

The out-of plane magnetization (figure 4.11) present a quite narrow hysteresis, with a saturating magnetic field of $0.3\,T$. This behaviour is typical of a ferromagnetic ordering, and was previously reported in literature, using different techniques[20, 22].
The magnetization curve in figure 4.12, taken with the photon beam at 75° from the c axis direction, couples the ferromagnetic contribution at low B field of the out-of plane direction, which presents an hysteresis at low field terminating at $0.8\,T$, and the magnetic behaviour of the basal plane, with a metamagnetic transition around $2.5\,T$. A more defined metamagnetic transition is found in the in-plane magnetization at the temperature of $4\,K$, reported in figure 4.13. The curve present a seemingly paramagnetic behaviour at low B, followed by a metamagnetic transition around $1.5\,T$. During the metamagnetic transition, an hysteresis opens. It is interesting to notice that, unlike many squid measurements [22, 32], no hysteresis is present at zero field. This fact indicates that the Ru moments do not undergo a ferromagnetic ordering in the basal plane for $B < 1.5\,T$. During the metamagnetic transition the anisotropy energy of the magnetic domains is overwhelmed by the strength of the magnetic field, and a ferromagnetic order is established. The presence of hysteresis in the metamagnetic regime indicates that a work is required to restore the demagnetized configuration, and can be explained in the context of magnetic domain structures. In particular, the coercive field required to recollect the metamagnetic transition, after reaching the saturation, can be related to the extra work required to rotate as a whole the aligned domains. The hysteresis found at zero field in literature[22] can be imputed either to samples with low degree of purity, where defects may prevent the sample from returning to the demagnetized configuration, or to the non precise alignment of the Hall probe with respect to the ab plane, which may leads to a residual out-of plane magnetization. Energy-dispersive-spectroscopy measurements, made after the XMCD experiments reveals that, in the region studied of our sample, the degree of purity was very high, and especially no other crystalline phases were present[33]. The metamagnetic transition changes with temperature, as can be seen from figure 4.14, and shifted to low B with increasing the disorder due to thermal fluctuation.

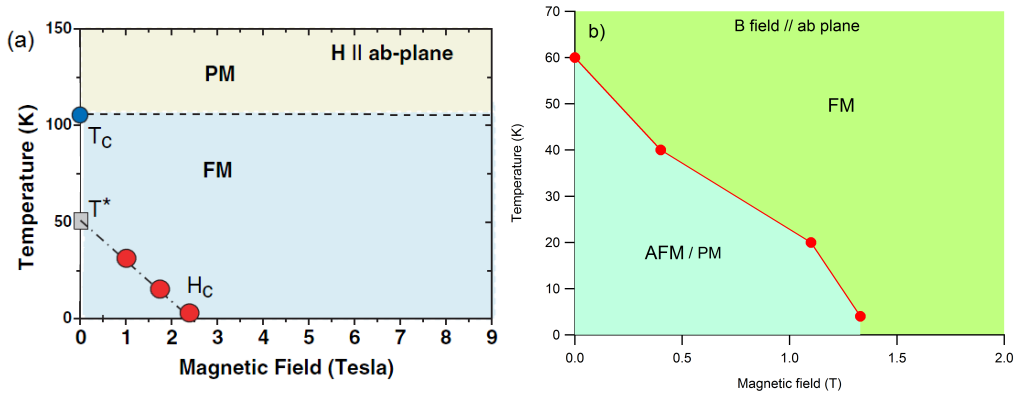


Figure 4.15: *Comparison between previously reported data[19], (a), and our results, (b).*

Already at $20\,K$, no hysteresis is visible in the metamagnetic transition, probably because thermal fluctuations participate in the spins orientation, so less work is needed to align magnetic moments. The light blue curve shows that at $60\,K$ the metamagnetic transition is no more present, and the system becomes magnetized already with a very small applied external field. We can make a phase diagrams of these results, and compare it to that already shown in section 1.2.3, and here reproposed in figure 4.15. Here we can see that the metamagnetic transition in our measurements occurs at low magnetic field intensities, compared to the values reported in ref.*[19]*.

The negligible XMCD signal on the L_3 edge (reported in figure 4.10(b)), due to the low polarization rate of the beam at this energy range, prevented any numerical calculation from the signal comparison at the two edges[3] .

[3]From the values of the XMCD intensity at the two absorption edges, it is possible to extract quantitative informations about the magnetization of Ru atoms, as the effective orbital and spin magnetic moment per atom. For more details see Ref.[25] or Ref.[34].

4.3 RXES data analysis

We made use of the RXES technique to study the overlapping of the $O\,2p - Ru\,3d$ orbitals in the $Sr_4Ru_3O_{10}$ compound. The electronic structure of $Sr_4Ru_3O_{10}$ obtained with the RXES data was then compared to the single layer structure of Sr_2RuO_4, taken as the reference compound.

The room temperature polarization-dependent spectra were resonantly measured across the O K-edge, in an energy range between $525-540\,eV$ for the incoming photon.

4.3.1 X-ray absorption spectra

Absorption spectra at the O K-edge were measured in two different geometries for the incoming electric field E_{inc}, as shown in figure 4.16a). In the vertical polarization, E_{inc} lies in the ab plane, while for the horizontal polarization E_{inc} has a major projection along the c axis. These two configurations select different empty final states, due to the different selection-rule symmetries. Figure 4.16b) represents the XAS spectra for the two different geometries, for the Sr_2RuO_4 and $Sr_4Ru_3O_{10}$ compounds. Experimental spectra are presented after a linear background subtraction and an intensity normalization far away from the absorption edge, and are referred to previously known spectra of the same samples.

The energy range of the X-ray absorption spectra can be divided in three main regions: the first ($\sim 4\,eV$ around the absorption threshold, located at $E_0 \simeq 528\,eV$) is attributed to $O\,2p$ empty states hybridized with $Ru\,4d$ t_{2g} and e_g empty states, while the second and the third regions, at higher energies, are attributed to the hybridization of $O\,2p$ empty states with $Sr\,4d$ and $Ru\,5sp$ states respectively [35, 36].
By comparing the low energy range (0-1 eV) XAS spectral line shape for the two different compounds, we found that the spectral weight is increased in intensity from $n = 1$ (Sr_2RuO_4) to $n = 3$ ($Sr_4Ru_3O_{10}$), for the in-plane polarization, and it's decreased after. The out-of-plane spectra, i.e. for the horizontal polarization, instead, are quite similar. The vertical polarization XAS spectrum of Sr_2RuO_4 presents two features in the low energy shape,

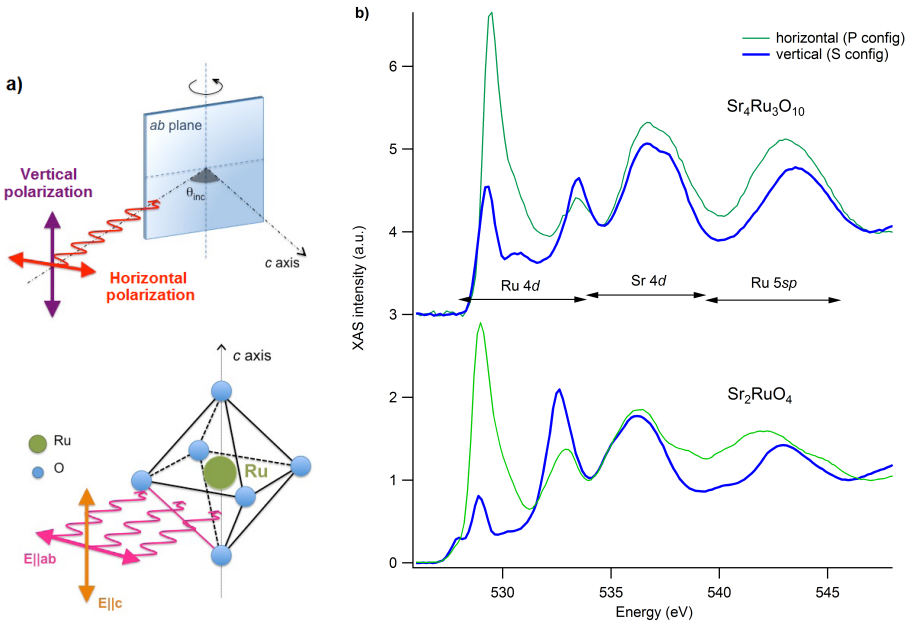


Figure 4.16: *a): different polarizations of the electric field select different states inside the Ru octahedron. Adapted from Ref.[35]. b): comparison between the two measured O K-edge XAS for the two geometries, for both the samples studied.*

which can be attributed to the non-equivalent apical and planar oxygen $1s$ core levels [36].

4.3.2 RXES spectra

We took emission spectra in the energy range between $525-540\,eV$, above the absorption threshold. The X-ray emission spectra were acquired for 13 energy points (see the red dots in figure 4.17, for Sr_2RuO_4) across the O K-edge. For every energy point, a spectra of 30 min long has been taken, for both polarization configurations. The RXES spectra are shown in figure 4.18. Spectra are aligned with respect to the incident photon energy, marked by the elastic peak in the S geometry (vertical polarization), after a constant background subtraction, due to the noise of the CCD, and an integral area normalization, so that each spectrum is proportional to the single electron decay probability.

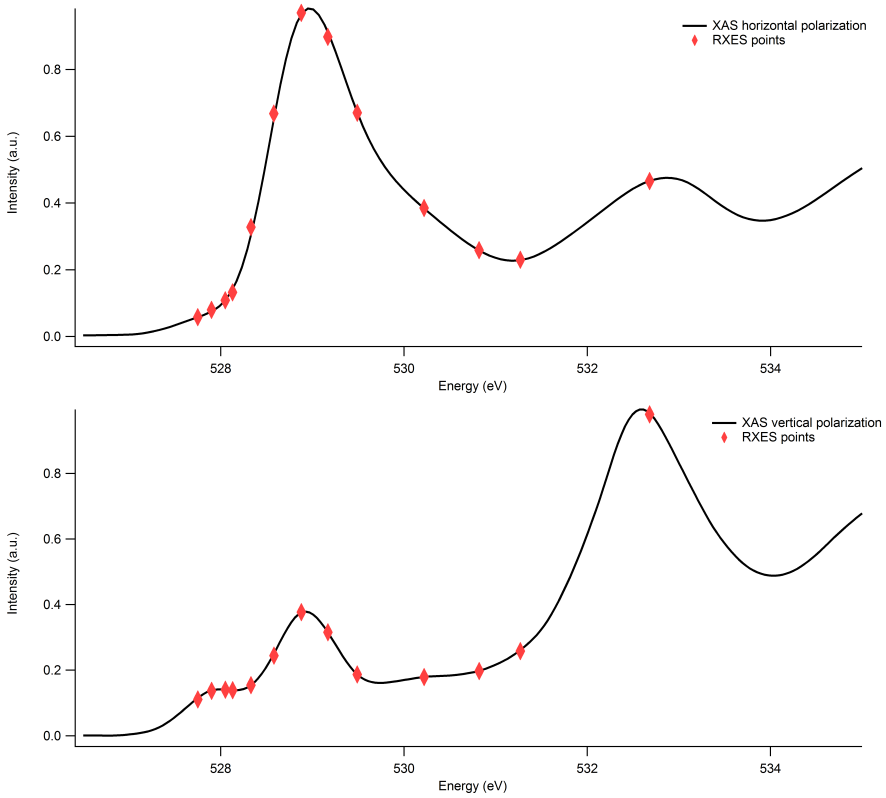


Figure 4.17: *Energy points for the X-ray emission spectra of Sr_2RuO_4 on the top of the absorption spectra.*

Starting from the spectrum at $560\,eV$, i.e. well above the absorption threshold, where the hybridization between $O\,2p$ and $Ru\,4d$ is null, we can see that at lower energies spectra assume a different profile. In particular, the intensity of the left shoulder (at lower photon energy) increases resonantly in a well delimited energy range. That is different for the two polarizations, and seems to last longer in the vertical configuration.

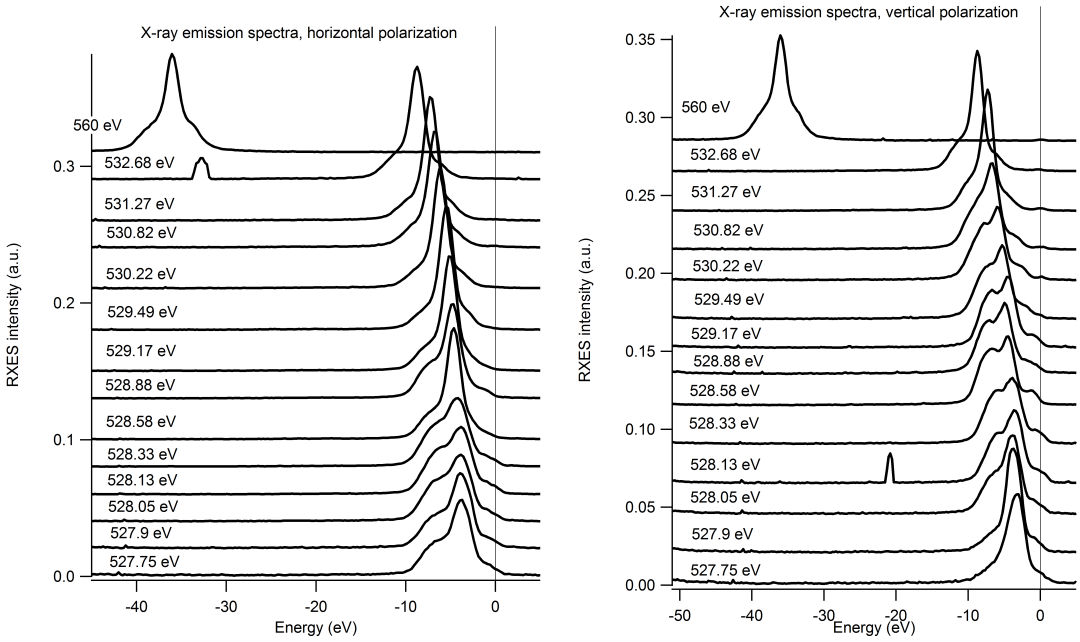


Figure 4.18: *RXES data of Sr_2RuO_4 for the two different incoming photon polarizations.*

The analysis of the intensity evolution and of the energy range of the resonant peak was carried out by using a fitting function with three Voigt profiles[4]. Each Voigt represents a feature of the emission spectrum, as shown in figure 4.19. We use a first fitting procedure with all the parameters left free, in order to have a first set of fitting values over the whole set of spectra, for each polarization. Then we calculate the mean values for the reciprocal positions of the three profiles, and for the Gaussian and Lorentzian line shapes. We used these results to fit the spectra with the three peak intensities as the only free values. We finally compared the rate between the peak intensity of the Voigt associated to the resonant excitation and that of the central peak, that we assumed to be independent from the resonance. Results for the two polarization are reported in the lower panel of figure 4.20.

[4]The Voigt profile is a convolution between a Gaussian and a Lorentzian profile. Each Voigt has then two "line-profile" parameters plus an intensity value and an energy position. The total fitting function has also a constant background parameter, which means 15 free parameters.

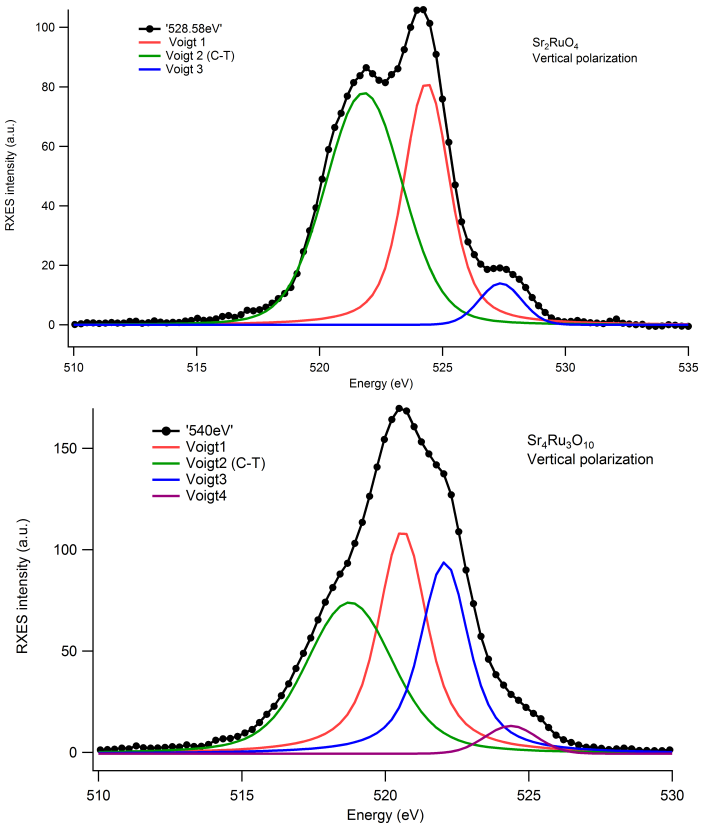


Figure 4.19: *Example of a fit with Voigt profiles. Up: a Sr_2RuO_4 spectrum with three Voigt. Down: a $Sr_4Ru_3O_{10}$ spectrum with four Voigt. The functions in green are simulating the resonant excitation.*

$Sr_4Ru_3O_{10}$ spectra have been fitted in a similar way, but we made use of four Voigt profiles, because data were more complicated in shape and a three Voigt function couldn't fit the spectra well enough (see figure 4.19 right). Results are plotted in the upper part of figure 4.20. Here we divided the resonant intensity for the mean value of the intensity of the two central Voigt, which didn't present any particular trend in energy.

Comparing the reported results, we can see that in both materials the resonant excitation covers a wider energy range in the vertical polarization data with respect to the horizontal polarization. In $Sr_4Ru_3O_{10}$, then, the excitation for both the polarizations starts at higher energy and it's wider in range, with respect to the other compound. The resonant energy shift is

consistent with the energy shift found in the X-ray absorption spectra, as in figure 4.16, while the larger energy range is due to the broader $p-$DOS of the $Sr_4Ru_3O_{10}$ with respect to Sr_2RuO_4. These difference is directly related to the differences of the crystalline structures in the two compounds, as discussed in the following paragraph.

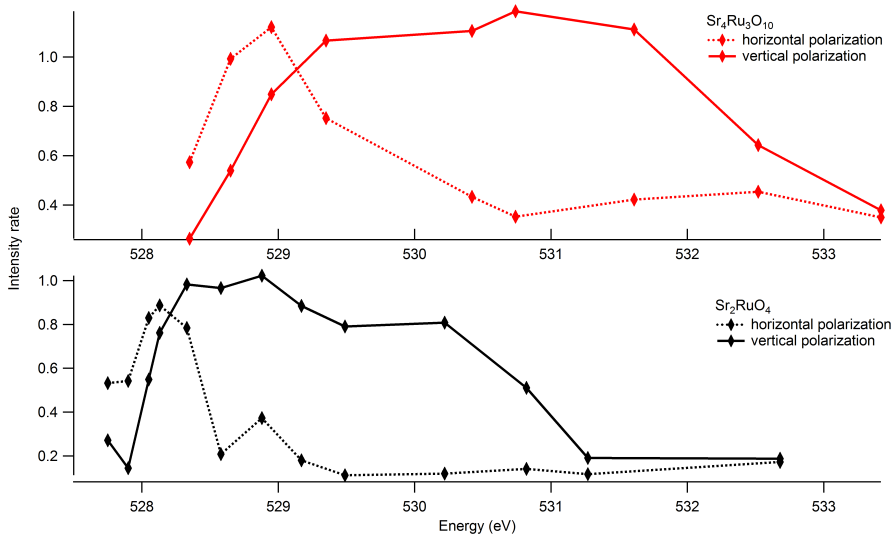


Figure 4.20: *Intensity rate (resonant Voigt / Central Voigt). Dashed lines between points are used for the horizontal polarization data, solid lines are for vertical polarization.*

4.3.3 Comparison between RXES spectra and simulated DOS

We have seen in section 2.3.1 that an X-ray emission spectrum depends on the DOS of the sample, apart from the matrix elements and other factors that determine the probability of the emission at a particular energy. Nevertheless, it is possible to compare the emitted photon energy with the position of the occupied states, and the resonant range in the absorption spectra with the empty states. We first make use of previously calculated DOS of the valence band[37] to see how the Ru atom forms bonds with the apical and planar oxygens. In figure 4.21(a) we display the total DOS of the two non equivalent oxygens and of the Ru atom of a single octahedron in Sr_2RuO_4,

with the principal chemical bonds underlined. We can see that the planar oxygen uses the p_x orbital (directed toward the ruthenium atom) to form a well defined bond with the $d_{x^2+y^2}$ of Ru. The apical oxygen, instead, binds to the Ru d_{z^2} with the p_z orbital, at higher energy. About $6\,eV$ below the Fermi energy, there is a broad hybridization between the t_{2g} orbitals of Ru and the p orbitals of the planar oxygen displaced perpendicularly to the $Ru-O$ direction (i.e. along y and z). From comparing the resonating structure of the XES spectra to the calculated DOS (see figure 4.21(b)) we can disentangle the contribution of the different orbital bonding symmetries. In particular, the low energy shoulder corresponds to the $p_x - p_z$ DOS of the planar oxygen, while the non resonating peak corresponds to the p_z orbital of the apical oxygen. Figure 4.22 shows the empty p-DOS of the planar and apical oxygens inside the octahedron, for the first three member of the R-P series. Comparing the black and the green DOS, belonging respectively to the Sr_2RuO_4 and $Sr_4Ru_3O_{10}$ compound, we can see that the energy range of the $Sr_4Ru_3O_{10}$ $p-$DOS is broader with respect to Sr_2RuO_4, especially for the apical oxygens. Differences in the crystal structure are directly reflected in the DOS, and in particular the DOS gets broader with increasing the number of layer, which increase the number of inequivalent oxygens inside the unit cell (4 in Sr_2RuO_4, 12 in $Sr_4Ru_3O_{10}$).

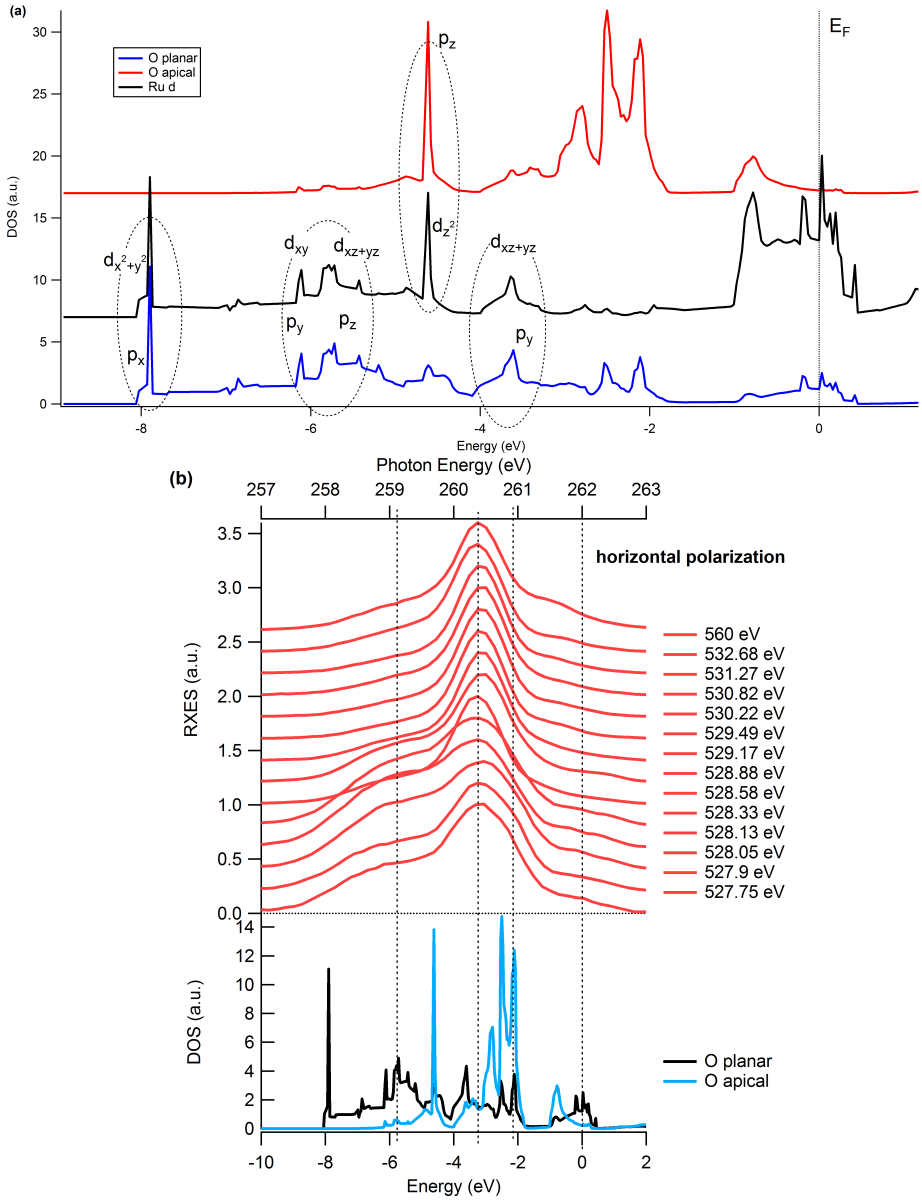


Figure 4.21: *(a): simulated valence DOS. Labels refer to simulations of the single atomic orbitals, not shown. (b): comparison between emission spectra of* Sr_2RuO_4 *and oxygens DOS. The resonant excitation seems to be related to the planar oxygen band located at* $6\,eV$*. Emission spectra here are been normalized with respect to their maximum intensity, in order to mark the resonant intensity evolution; their energy position has to be doubled, because data are taken in second order diffraction.*

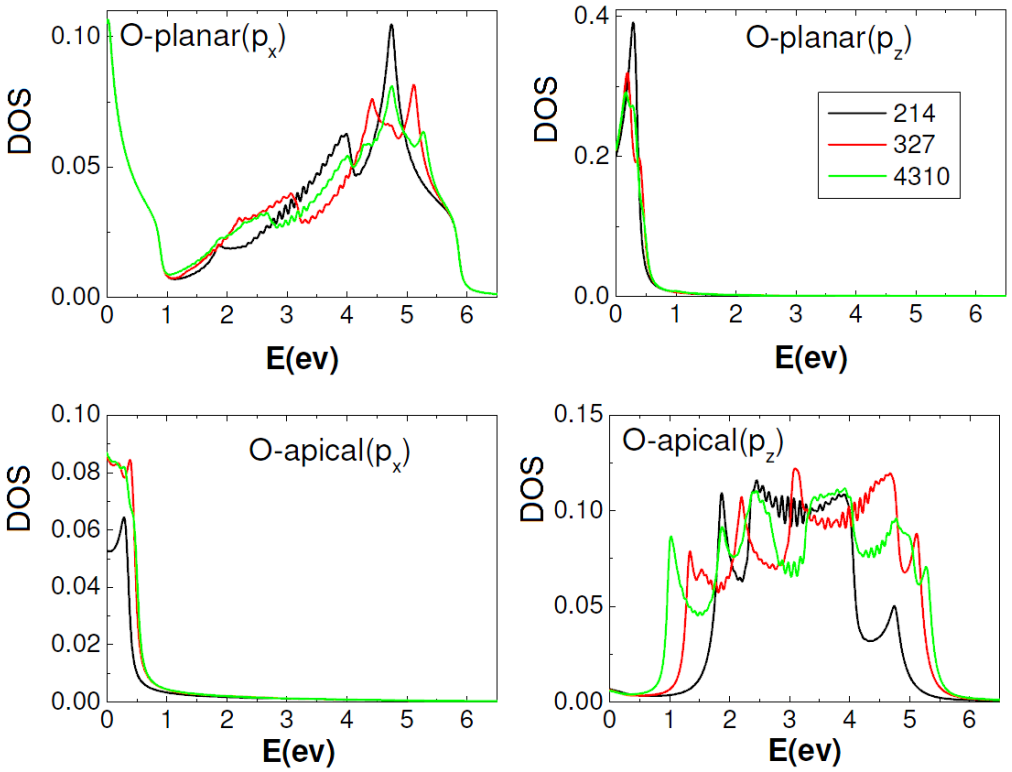


Figure 4.22: *Comparison between simulated empty p-DOS of the oxygens atoms, for the first three members of the R-P series. Image adapted from Ref.[37].*

Chapter 5

Conclusions

This thesis is the starting point of a research project that has the aim of combining standard state-of-the-art synchrotron X-ray absotrpion and resonant X-ray emission spectroscopies with time resolved laser reflectivity for exploring unconventional phenomena due to a subtle interplay between orbital anisotropy, multi-band effects, magnetic fluctuations and dimensionality in strongly electron correlated materials. The combination of all these techniques should give an extended view of the electronic and magnetic structures and their coupling to the dynamical properties of the system under investigation. To reach this goal, this multidisciplinary approach has been applied to an intriguing class of layered oxides, the R-P type ruthenates series, which display a very peculiar range of physical properties as a function of the number of RuO_2 layers.

The main results of this thesis are: the time dependent thermal trend of the differential reflectivity of $Sr_3Ru_2O_7$ has been measured for the first time in its Fermi Liquid and non Fermi Liquid phases. We saw that in the FL regime, at low temperature, a single exponential decay mechanism can be used to describe the scattering process, like in the case of a simple metal. In the NFL regime, instead, two distinct decay mechanism are present in the thermalization process: a fast decay, which reaches a scattering rate of $8\,ps^{-1}$ at room temperature, and a slow decay rate ($\sim 2\,ps^{-1}$). Only the slow decay recollects the transition occurring at $250\,K$, reproducing the behaviour of

the static measurements in literature. The offset parameter was not affected by this transition, but showed a strong enhancement below $50\,K$, where the FL-NFL transition take place. Time resolved reflectivity probed at different wavelengths in the infrared region showed that unequal behaviour is present for temperatures above and below the FL-NFL transition, and further measurements in the visible spectral region are required.

Magnetization curves taken at the $Ru\ L_2$ absorption edge of $Sr_4Ru_3O_{10}$ showed a magnetic behaviour similar to that reported in literature. Our results allow to add few points of the temperature phase diagram, in the region of the metamagnetic transition. We found that the resulting metamagnetic transition, as a function of the temperature, happens at lower B values with respect to literature data.

Resonance effects in the Sr_2RuO_4 and $Sr_4Ru_3O_{10}$ compounds take place in a different energy range, and in particular the resonances in $Sr_4Ru_3O_{10}$ last longer, because of the broader DOS of the compound. The broadening of the electronic states can be related to the inequivalent oxygens inside the unit cell. Finally, the incident electric field polarization has been seen to induce a different resonance mechanism, which can eventually be related to the hybridization between ruthenium and the apical or planar oxygens.

Appendix

Three-temperature model

The two-temperature model proposed in section 2.1 is a very simplified model, and takes into account only one global scattering mechanism between the already-thermalized exited electron population and the lattice. Experimental observations have shown, indeed, that this model is not able to reproduce the behaviour of certain anisotropic or strongly correlated materials [38, 39]. In these experiments, the authors showed that the excited electron gas at temperature T_e thermalized first with a small fraction of phonon modes, with a typical timescale of $10^2 ps$ (τ_α), leading to an effective temperature T_p, and then the scattering is extended to the whole lattice with a slower decay time τ_β. So after few picoseconds electrons and lattice has a global temperature T_l, and the dynamics of electrons and phonons become similar.

A quantitative description of the processes involved can be obtained solving an extended version of the TTM, also called three-temperature model. Using the nomenclature in section 2.1, the rate equations describing the time evolution of the three temperatures are [38]:

$$\begin{aligned}
\frac{\partial T_e}{\partial \tau} &= -\frac{3\lambda\Omega_0^3}{\hbar\pi k_B}\frac{n_e - n_p}{T_e} + \frac{P}{C_e} \\
\frac{\partial T_p}{\partial \tau} &= \frac{C_e}{C_p}\frac{3\lambda\Omega_0^3}{\hbar\pi k_B}\frac{n_e - n_p}{T_e} - \frac{T_p - T_l}{\tau_\beta} \\
\frac{\partial T_l}{\partial \tau} &= \frac{C_p}{C_l}\frac{T_p - T_l}{\tau_\beta}
\end{aligned}$$

where $n_{e,p} = \left(e^{\Omega/k_B T_{e,p}} - 1\right)^{-1}$ are the Bose-Einstein distribution for electrons and phonons, and P is the Gaussian profile of the laser pulse. The specific heat of electrons, strongly coupled phonons and lattice are, respectively, $C_e = \gamma T_e$, $C_p = 3f\Omega_0 \partial n_p/\partial T_p$, and $C_l = 3(1-f)\Omega_0 \partial n_p/\partial T_p$. Here, f is the fraction of phonon modes that are more strongly excited. In the coupling with the rest of the lattice, the temporal evolution of T_e has been neglected, because of the weak decay mechanism.

Bibliography

[1] J.G. Bednorz and K.A. Muller. *Z. Phys. B*, 64(189), 1986.

[2] Y. Tokura and N. Nagaosa. *Science*, 288:462, 2000.

[3] S.A. Grigera et al. *Science*, 306:1154, 2004.

[4] P. Fazekas. *Lecture notes on Electron Correlation and Magnetism*. World Scientific.

[5] R. Fittipaldi. *Superconductivity of the Sr2RuO4-Sr3Ru2O7 eutectic crystals grown by floating zone technique*. PhD thesis, Università degli Studi di Salerno, 2007.

[6] Y. Maeno et al. *Nature*, 372:532, 1994.

[7] A.P. Mackenzie and Y. Maeno. *Rev. Mod. Phys.*, 75(2), 2003.

[8] T. Bauer and C. Falter. *J. Phys.: Condens. Matter*, 21:395701, 2009.

[9] C. Noce et al. *Ruthenate and rutheno-cuprate materials*. Lecture Notes in Physics. Springer.

[10] N.E. Hussey et al. *Phys. Rev. B*, 57:611–614, 1998.

[11] S. Ikeda et al. *Phys. Rev. B*, 62(10), 2000.

[12] H. Shaked et al. *Phys. Rev. B*, 62(13), 2000.

[13] J. Hooper et al. *Phys. Rev. B*, 75:060403(R), 2007.

[14] K. Kitagawa et al. *Phys. Rev. Lett.*, 95:127001, 2005.

[15] M.B. Stone et al. *Phys. Rev. B*, 73:174426, 2006.

[16] L. Capogna et al. *Phys. Rev. B*, 67:012504, 2003.

[17] S.A. Grigera et al. *Phys. Rev. B*, 67:214427, 2003.

[18] R.S. Perry et al. *Phys. Rev. Lett.*, 86(12), 2001.

[19] R. Gupta et al. *Phys. Rev. Lett.*, 96:067004, 2006.

[20] W. Bao et al. cond-mat/0607428.

[21] M.N. Iliev et al. *Physica B*, 358:138, 2005.

[22] G. Cao et al. *Phys. Rev. B*, 68:174409, 2003.

[23] P.B. Allen. *Phys. Rev. Lett.*, 59, 1987.

[24] H. Kitty. *H.K. dalla A alla Z.* Edi Bimbi.

[25] J. Stöhr and H.C. Siegmann. *Magnetism From Fundamentals to Nanoscale Dynamics.* Springer.

[26] A. Kotani and S. Shin. *Rev. Mod. Phys.*, 73(1), 2001.

[27] http://www.esrf.eu/usersandscience/experiments/electstructmagn/id12.

[28] http://www.esrf.eu/usersandscience/experiments/electstructmagn/id12/old1996handbook.

[29] F. Bondino et al. *Phys. Rev. B*, 75:195106, 2007.

[30] H.M. Rogier et al. *Phys. Rev. B*, 45(9), 1991.

[31] C. Mirri et al. *Phys. Rev. B*, 78:155132, 2008.

[32] E. Carleschi. Private communication.

[33] R. Fittipaldi. Private communication.

[34] F. de Groot and A. Kotani. *Core Level Spectroscopy of Solids.*

[35] E. Carleschi. *Electronic structure of transition metal and rare earth ions in complex materials by resonant core-level spectroscopies.* PhD thesis, Università degli Studi di Trieste, 2007.

[36] M. Malvestuto et al. Paper in preparation.

[37] M. Malvestuto and E. Pavarini. Private communication.

[38] L. Perfetti et al. *Phys. Rev. Lett.*, 99:197001, 2007.

[39] T. Kamptfrath. *Phys. Rev. Lett.*, 95:187403, 2005.

Nomenclature

AFM Antiferromagnetic

BACH Beamline for Advanced diCHroism

CCD Charge-coupled device

CP Cyrcularly Polarized (photons)

DOS Density of states

e-e Electron-electron interaction

e-ph Electron-phonon

FM Ferromagnetic

NFL Non Fermi liquid

OPA Optical Parametric Amplifier

R-P Ruddlesden-Popper (series)

RegA Regenerative Amplifier

RXES Resonant X-ray Emission Spectroscopy

SM Sherical Mirror (usually numbered)

TMOs Transition metal oxides

TTM Two-temperature model

UHV Ultra-high vacuum

XES X-ray Emission Spectroscopy

XMCD X-ray Magnetic Cyrcular Dichroism

Grazie

Marco! Grazie per avermi supportato nel lavoro di tesi e sopportato al suo fianco durante il suo lavoro di ricerca. Grazie al prof. Parmigiani per avermi proposto e consigliato di intraprendere questo lavoro, e per avere delineato nel tempo l'evoluzione del progetto. Ringrazio Giacomo per l'indispensabile aiuto in laboratorio e con l'analisi dati, Federico per i consigli, Barbara per tutti i pasticci burocratici che solo lei riesce sempre a risolvere, Cesare per la musica, Valentina per la compagnia contornata da gatti stilizzati bianchi e rosa (vedi Ref.[24]) e i consigli stilistici (vedi figura 4.3(a)), e tutti gli altri membri del gruppo per il clima sempre allegro dell'open space. Grazie anche a tutto il gruppo per i momenti fuori dalle mura dell'area di ricerca, in particolare quando l'argomento "fisica" non veniva toccato (spesso, per fortuna)! Un ricordo e un grazie vanno anche alle "lontane" Rosalba (aka Tatiana) ed Emanuela per il bel periodo a Grenoble.